ALMA Lensing Cluster Survey: Physical Characterization of Near-infrared-dark Intrinsically Faint ALMA Sources at z = 2-4

The Astrophysical Journal, 989:115 (20pp), 2025 August 10 https://doi.org/10.3847/1538-4357/adb41d

ALMA Lensing Cluster Survey: Physical Characterization of Near-infrared-dark Intrinsically Faint ALMA Sources at $z = 2$–4

Akiyoshi Tsujita[1], Kotaro Kohno[1,2], Shuo Huang[3,4], Masamune Oguri[5,6], Ken-ichi Tadaki[7], Ian Smail[8], Hideki Umehata[4,9,10], Zhen-Kai Gao[11,12], Wei-Hao Wang[11], Fengwu Sun[13,14], Seiji Fujimoto[15,16,17], Tao Wang[18], Ryosuke Uematsu[19], Daniel Espada[20,21], Francesco Valentino[22,23], Yiping Ao[24,25], Franz E. Bauer[26,27,28], Bunyo Hatsukade[1,3,29], Fumi Egusa[1], Yuri Nishimura[1], Anton M. Koekemoer[30], Daniel Schaerer[31,32], Claudia Lagos[23,33,34], Miroslava Dessauges-Zavadsky[35], Gabriel Brammer[17,23], Karina Caputi[23,36], Eiichi Egami[14], Jorge González-López[37,38], Jean-Baptiste Jolly[39,40], Kirsten K. Knudsen[39], Vasily Kokorev[17,23,36], Georgios E. Magdis[23,41,42], Masami Ouchi[3,43,44], Sune Toft[17,23], John F. Wu[30,45], and Adi Zitrin[46]

[1] Institute of Astronomy, Graduate School of Science, The University of Tokyo, 2-21-1 Osawa, Mitaka, Tokyo 181-0015, Japan
[2] Research Center for the Early Universe, Graduate School of Science, The University of Tokyo, 7-3-1 Hongo, Bunkyo-ku, Tokyo 113-0033, Japan
[3] National Astronomical Observatory of Japan, 2-21-1 Osawa, Mitaka, Tokyo 181-8588, Japan
[4] Department of Physics, Graduate School of Science, Nagoya University, Furocho, Chikusa, Nagoya 464-8602, Japan
[5] Center for Frontier Science, Chiba University, 1-33 Yayoi-cho, Inage-ku, Chiba 263-8522, Japan
[6] Department of Physics, Graduate School of Science, Chiba University, 1-33 Yayoi-Cho, Inage-Ku, Chiba 263-8522, Japan
[7] Graduate School of Engineering, Hokkai-Gakuen University, 1-1, Nishi 11-chome, Minami 26-jo, Chuo-ku, Sapporo-shi, Hokkaido 064-0926, Japan
[8] Centre for Extragalactic Astronomy, Department of Physics, Durham University, South Road, Durham DH1 3LE, UK
[9] Institute for Advanced Research, Nagoya University, Furocho, Chikusa, Nagoya 464-8602, Japan
[10] Cahill Center for Astronomy and Astrophysics, California Institute of Technology, 1200 E California Boulevard, MC 249-17, Pasadena, CA 91125, USA
[11] Institute of Astronomy and Astrophysics, Academia Sinica, Taipei 10617, Taiwan
[12] Graduate Institute of Astronomy, National Central University, Zhongli, Taoyuan 32001, Taiwan
[13] Center for Astrophysics | Harvard & Smithsonian, 60 Garden Street, Cambridge, MA 02138, USA
[14] Steward Observatory, University of Arizona, 933 N. Cherry Avenue, Tucson, AZ 85721, USA
[15] Department of Astronomy, The University of Texas at Austin, Austin, TX, USA
[16] Cosmic Dawn Center (DAWN), Jagtvej 128, DK2200 Copenhagen N, Denmark
[17] Niels Bohr Institute, University of Copenhagen, Jagtvej 128, DK2200 Copenhagen N, Denmark
[18] Key Laboratory of Modern Astronomy and Astrophysics (Nanjing University), Ministry of Education, Nanjing 210093, People's Republic of China
[19] Department of Astronomy, Kyoto University, Kyoto 606-8502, Japan
[20] Departamento de Física Teórica y del Cosmos, Campus de Fuentenueva, Edificio Mecenas, Universidad de Granada, E-18071, Granada, Spain
[21] Instituto Carlos I de Física Teórica y Computacional, Facultad de Ciencias, E-18071, Granada, Spain
[22] European Southern Observatory, Karl-Schwarzschild-Str. 2, D-85748, Garching, Germany
[23] Cosmic Dawn Center (DAWN), Denmark
[24] Purple Mountain Observatory and Key Laboratory for Radio Astronomy, Chinese Academy of Sciences, Nanjing, People's Republic of China
[25] School of Astronomy and Space Science, University of Science and Technology of China, Hefei, People's Republic of China
[26] Instituto de Astrofísica, Facultad de Física, Pontificia Universidad Católica de Chile, Campus San Joaquín, Av. Vicuña Mackenna 4860, Macul Santiago, 7820436, Chile
[27] Centro de Astroingeniería, Facultad de Física, Pontificia Universidad Católica de Chile, Campus San Joaquín, Av. Vicuña Mackenna 4860, Macul Santiago, 7820436, Chile
[28] Millennium Institute of Astrophysics, Nuncio Monseñor Sótero Sanz 100, Of 104, Providencia, Santiago, Chile
[29] Graduate Institute for Advanced Studies, SOKENDAI, Osawa, Mitaka, Tokyo 181-8588, Japan
[30] Space Telescope Science Institute, 3700 San Martin Drive, Baltimore, MD 21218, USA
[31] Observatoire de Genéve, Université de Genéve, 51 Ch. des Maillettes, 1290 Versoix, Switzerland
[32] CNRS, IRAP, 14 Avenue E. Belin, 31400 Toulouse, France
[33] International Centre for Radio Astronomy Research (ICRAR), M468, University of Western Australia, 35 Stirling Highway, Crawley, WA 6009, Australia
[34] ARC Centre of Excellence for All Sky Astrophysics in 3 Dimensions (ASTRO 3D), Australia
[35] Department of Astronomy, University of Geneva, Chemin Pegasi 51, 1290 Versoix, Switzerland
[36] Kapteyn Astronomical Institute, University of Groningen, P.O. Box 800, 9700AV Groningen, The Netherlands
[37] Núcleo de Astronomía de la Facultad de Ingeniería y Ciencias, Universidad Diego Portales, Av. Ejército Libertador 441, Santiago, Chile
[38] Las Campanas Observatory, Carnegie Institution of Washington, Casilla 601, La Serena, Chile
[39] Department of Space, Earth and Environment, Chalmers University of Technology, Onsala Space Observatory, SE-43992 Onsala, Sweden
[40] Max-Planck-Institut für extraterrestrische Physik, 85748 Garching, Germany
[41] DTU-Space, Technical University of Denmark, Elektrovej 327, 2800, Kgs. Lyngby, Denmark
[42] Niels Bohr Institute, University of Copenhagen, Jagtvej 128, 2200, Copenhagen N, Denmark
[43] Institute for Cosmic Ray Research, The University of Tokyo, 5-1-5 Kashiwanoha, Kashiwa, Chiba 277-8582, Japan
[44] Kavli Institute for the Physics and Mathematics of the Universe (WPI), University of Tokyo, Kashiwa, Chiba 277-8583, Japan
[45] Center for Astrophysical Sciences, Johns Hopkins University, 3400 N Charles Street, Baltimore, MD 21218, USA
[46] Physics Department, Ben-Gurion University of the Negev, P.O. Box 653, Be'er-sheva 8410501, Israel
Received 2024 June 14; revised 2025 February 3; accepted 2025 February 7; published 2025 August 7

Abstract

We present results from Atacama Large Millimeter/submillimeter Array (ALMA) spectral line-scan observations at 3 mm and 2 mm bands of three near-infrared-dark (NIR-dark) galaxies behind two massive lensing clusters

MACS J0417.5-1154 and RXC J0032.1+1808. Each of these three sources is a (sub)millimeter faint (delensed $S_{1.2\,\mathrm{mm}} < 1$ mJy) triply lensed system originally discovered in the ALMA Lensing Cluster Survey. We have successfully detected CO and [C I] emission lines and confirmed that their spectroscopic redshifts are $z = 3.652$, 2.391, and 2.985. By utilizing a rich multiwavelength data set, we find that the NIR-dark galaxies are located on the star formation main sequence in the intrinsic stellar mass range of $\log(M_*/M_\odot) = 9.8$–10.4, which is about 1 order of magnitude lower than that of typical submillimeter galaxies (SMGs). These NIR-dark galaxies show a variety in gas depletion times and spatial extent of dust emission. One of the three is a normal star-forming galaxy with gas depletion time consistent with a scaling relation, and its infrared surface brightness is an order of magnitude smaller than that of typical SMGs. Since this galaxy has an elongated axis ratio of ∼0.17, we argue that normal star-forming galaxies in an edge-on configuration can be heavily dust-obscured. This implies that existing deep WFC3/F160W surveys may miss a fraction of typical star-forming main-sequence galaxies due to their edge-on orientation.

Unified Astronomy Thesaurus concepts: Starburst galaxies (1570); High-redshift galaxies (734); Strong gravitational lensing (1643); Millimeter-wave spectroscopy (2252)

1. Introduction

Dust affects the spectral energy distribution (SED) of galaxies by absorbing and scattering ultraviolet (UV) and optical emission, mainly produced by young stars, and reemitting the energy at the far-infrared (FIR) and submillimeter wavelengths. Consequently, dusty galaxies at $z \gtrsim 2$ typically appear very faint at observed-frame optical/near-infrared (NIR) due to dust obscuration. Instead, their dust continuum is prominent at FIR/submillimeter band and some extreme ones are bright enough (e.g., $S_{870\,\mu\mathrm{m}} >$ several mJy) to be detected with single-dish telescopes. They are referred to as submillimeter galaxies (SMGs; J. A. Hodge & E. da Cunha 2020 for a review). Since the first detection of high-redshift SMGs, many have been found to be completely obscured in the rest-frame UV/optical (or observed-frame NIR) due to strong dust attenuation, dubbed near-infrared-dark (NIR-dark) galaxies (e.g., I. Smail et al. 1999, 2021; E. da Cunha et al. 2015; C. M. Casey et al. 2019; Y. Yamaguchi et al. 2019; U. Dudzevičiūtė et al. 2020; D. A. Riechers et al. 2020; H. Umehata et al. 2020; F. Sun et al. 2021; J. A. Zavala et al. 2021; X. Shu et al. 2022). Similar terms, such as HST-dark and H/K-dropout, are also used to describe these dust-obscured sources.

The advent of the Atacama Large Millimeter/submillimeter Array (ALMA) has enabled us to uncover the faint ($S_{1.2\,\mathrm{mm}} < 1$ mJy) (sub)millimeter-selected galaxies, that are significantly fainter (up to ∼100 times) than the classical SMGs. Hereafter, we will use the term dusty star-forming galaxies (DSFGs) to more generally refer to dusty galaxies including these faint sources. It has been revealed that the dust-obscured galaxies exist not only among SMG-like extreme starburst galaxies but also among more common DSFGs that lie on the main sequence of the M_*–SFR relation (C. Schreiber et al. 2015), particularly at the high mass end where $M_* > 10^{10.3}\,M_\odot$ (e.g., T. Wang et al. 2019). These galaxies have been detected through blind ALMA surveys (e.g., J. M. Simpson et al. 2014; S. Fujimoto et al. 2016, 2023, 2024; Y. Yamaguchi et al. 2016, 2019; M. Franco et al. 2018; U. Dudzevičiūtė et al. 2020; C. Gruppioni et al. 2020; M. Y. Xiao et al. 2023), follow-up ALMA observations of galaxies with very red colors in the NIR range (e.g., K. I. Caputi et al. 2012; T. Wang et al. 2016, 2019; B. Alcalde Pampliega et al. 2019), follow-up ALMA observations of strongly lensed galaxies that are identified in (sub)millimeter-single-dish surveys (A. Pope et al. 2017, 2023; X. Shu et al. 2022; A. Mizener et al. 2024), and serendipitous discoveries (B. Hatsukade et al. 2015; C. C. Williams et al. 2019; M. Romano et al. 2020; Y. Fudamoto et al. 2021). Recent James Webb Space Telescope (JWST) observations have also begun to uncover a broader range of NIR-dark galaxies, including those that are less massive (e.g., L. Barrufet et al. 2023, 2025; C. Gómez-Guijarro et al. 2023; V. Kokorev et al. 2023; J. McKinney et al. 2023a; E. J. Nelson et al. 2023; P. G. Pérez-González et al. 2023; I. Smail et al. 2023; F. Sun et al. 2024; M. Xiao et al. 2024).

This normal dust-obscured population was often missed by previous (sub)millimeter-single-dish surveys due to its modest (sub)millimeter flux, lower than the confusion limit of single-dish telescopes, and was also overlooked by the Lyman break technique, which relies on the rest-frame UV light. However, T. Wang et al. (2019) suggested that this population constitutes the bulk of massive galaxies (from 20% at $M_* \sim 10^{10.3}\,M_\odot$ to 80% at $M_* \sim 10^{11.0}\,M_\odot$) at $z \sim 3$–6 and is the main progenitor of the most massive quiescent galaxies at $z \sim 2$–3, as well as of today's ellipticals that reside in the central regions of massive groups and clusters (see also F. Valentino et al. 2020). The large number of such dusty massive galaxies in the early universe is not accounted for by current semianalytical models, posing a challenge to our understanding of massive galaxy formation.

Despite its importance, obtaining accurate redshifts for these galaxies (either optical/NIR spectroscopy or (sub)millimeter line scans) is challenging, hindering efforts to characterize the population. This difficulty is partly due to significant extinction in the rest-frame UV and optical, where key redshift indicators like the Lyman break and 4000 Å break lie. Another factor is the significantly lower (sub)millimeter flux of this population compared with those of classical SMGs, which makes line scan observations for redshift search much more expensive, even with ALMA. To date, several spectroscopic redshift identifications for the NIR-dark galaxies have been reported (e.g., A. M. Swinbank et al. 2012; C. M. Casey et al. 2019; C. C. Williams et al. 2019; D. A. Riechers et al. 2020; H. Umehata et al. 2020; L. Zhou et al. 2020; V. Kokorev et al. 2023; I. Smail et al. 2023; F. Sun et al. 2024; L. Barrufet et al. 2025), but almost all of them are for the SMG-class bright sources except for a few cases, such as Y. Fudamoto et al. (2021), which reported the serendipitous $[\mathrm{C\,II}]_{158}$ line detection of two normal dust-obscured galaxies at $z \sim 7$. Therefore, physical characterizations based on secure redshifts remain largely unexplored for the normal NIR-dark population,

particularly in terms of molecular gas properties based on CO or [C I] emission lines.

Furthermore, it remains unclear what the origin of the strong dust attenuation is, or in other words, what differentiates NIR-dark galaxies from other normal main sequence SFGs. I. Smail et al. (2021) investigated the correlation between the strength of dust attenuation (A_V) and other physical quantities in ALMA-identified SMGs, concluding that the correlations with dust mass and stellar mass are weak, while those with the photometric redshift and the "compactness" of the star-forming region ($\Sigma_{\rm IR}$) show stronger links. However, they suggest that other factors such as the geometry of stars/dust may also be involved, particularly for completely dust-obscured galaxies (see also E. da Cunha et al. 2015; W. Wang et al. 2018; R. Cochrane et al. 2024). Moreover, recent JWST studies claim that the viewing angle of the galaxy (i.e., an edge-on disk) may be a contributing factor (E. J. Nelson et al. 2023), while others argue that redshift and/or stellar mass are the main factors (C. d. P. Lagos et al. 2020; C. Gómez-Guijarro et al. 2023; B. Lorenz et al. 2023).

In this paper, we focus on normal dust-obscured galaxies originally discovered in the ALMA Lensing Cluster Survey (ALCS). Thanks to lens magnification, these galaxies appear as bright as classic SMGs (detectable with typical single-dish telescopes), making them suitable for follow-up observations. We successfully identified spectroscopic redshifts for three sources and estimated their basic physical properties via ALMA Band 3 and 4 line scan observations. We then compared these properties with those of other galaxy populations. Based on the obtained results, we discuss the evolutionary scenario and the origin of the strong dust attenuation for the normal dust-obscured galaxies.

This paper is organized as follows. Section 2 describes the observational data and reduction. In Section 3, we present the spectral redshift identification, SED fitting results, molecular gas properties, FIR morphology, and properties of the photodissociation region of our samples. In Section 4, we discuss the origin of the strong dust attenuation. A summary is presented in Section 5. Throughout the paper, we adopt a cosmology with $\Omega_m = 0.3$, $\Omega_\Lambda = 0.7$, and $H_0 = 70\,{\rm km\,s^{-1}\,Mpc^{-1}}$ and the Chabrier initial mass function (IMF; G. Chabrier 2003). We convert values obtained by other studies from the E. E. Salpeter (1955) IMF to the Chabrier IMF by dividing SFR and stellar masses by the same factor, 1.7 (J. S. Speagle et al. 2014). All magnitudes in this paper are expressed in the AB system (J. B. Oke 1974).

2. Data and Reduction

2.1. ALMA Lensing Cluster Survey

The ALMA Lensing Cluster Survey (ALCS; K. Kohno et al. 2023; S. Fujimoto et al. 2024) is a Cycle-6 ALMA large program (project code: 2018.1.00035.L; PI: K. Kohno) that targets highly magnified areas within 33 massive galaxy clusters. The samples are selected from the best-studied clusters drawn from the Cluster Lensing And Supernova Survey with Hubble (CLASH; M. Postman et al. 2012), Hubble Frontier Fields (HFF; J. M. Lotz et al. 2017), and the Reionization Lensing Cluster Survey (RELICS; D. Coe et al. 2019). The survey employs a 15 GHz-wide spectral scan in Band 6 ($\overline{\lambda_{\rm obs}} = 1.15$ mm, $\overline{\nu_{\rm obs}} = 260$ GHz). The total mapping area reaches 134 arcmin^2 (primary beam > 0.3) with a typical noise level of $1\sigma \sim 60\,\mu{\rm Jy\,beam^{-1}}$. Thanks to cluster lensing, ALCS explores a unique parameter space toward faint and wide regimes, compared to existing ALMA deep surveys.

Observations were carried out between 2018 December and 2019 December in compact array configurations of C43-1 and C43-2 (corresponding to a beam size of $\theta \sim 1''$) fine-tuned to recover strongly lensed (i.e., spatially elongated), low surface brightness sources. ALCS yields 180 continuum source detections in total (including multiple images) consisting of 141 blind detections with a signal-to-noise ratio (SNR) of greater than five in the natural weighting maps and 39 prior-based detections with SNR = 4–5 that have IRAC-counterparts. Full descriptions of the data analysis and source catalog are given in S. Fujimoto et al. (2024).

2.2. Optical, NIR, and FIR Catalogs

The 33 clusters were observed with HST, Spitzer Space Telescope, and Herschel Space Observatory.

V. Kokorev et al. (2022) build a set of HST and Spitzer/IRAC 3.6 and 4.5 μm mosaics and photometric catalogs by reprocessing archival data in the ALCS fields. One of the difficulties in studying the galaxy clusters and other crowded regions is that the photometries taken by low-resolution instruments such as Spitzer/IRAC suffer from the effect of blending. To alleviate the effect, they model the Spitzer photometry by convolving the HST detection image with the Spitzer PSF using the novel `GOLFIR` software.

F. Sun et al. (2022) compile archival data from Herschel/PACS and SPIRE observations of the 33 clusters, with most of the data coming from the Herschel Lensing Survey (E. Egami et al. 2010). The study includes data taken at 100 and 160 μm with PACS, and 250, 350, 500 μm with SPIRE. Given the coarse angular resolution of Herschel (typical beam sizes are $7\farcs4$ and $11\farcs4$ for the 100 and 160 μm bands of PACS, and $18''$, $24''$, and $35''$ for the 250, 350, and 500 μm bands of SPIRE), the authors deblended the Herschel fluxes using secure ALMA detections from the ALCS as priors.

2.3. Target Selection

In this work, we define NIR-dark sources as those with $H - [4.5] > 2.3$, which are extremely red objects with H-band (F160W-band) and IRAC 4.5 μm channel color, following the traditional method described in T. Wang et al. (2016). This color selection is designed to complementarily select massive star-forming galaxies that are systematically missed by the Lyman break selection, which is specifically designed to select young and less attenuated galaxies (e.g., R. J. Bouwens et al. 2012).

Figure 1 presents the color–magnitude diagram ($H - [4.5]$ versus [4.5]) for the ALCS sample. We exclude sources that are not covered in the H-band, those contaminated by nearby bright objects or other artificial factors, or those identified as IRAC-dropout. Among the NIR-dark objects, six are H-dropout or HST-dark. We calculated the lower limit of their H-band magnitude by taking three times the median uncertainty of all photometric measurements within the corresponding galaxy cluster region in the V. Kokorev et al. (2022) catalog. In the V. Kokorev et al. (2022) catalogs, the IRAC photometries are measured by convolving the HST detection image with the IRAC PSF. The IRAC photometries of the HST-dark sources are instead measured using a $D = 3''$

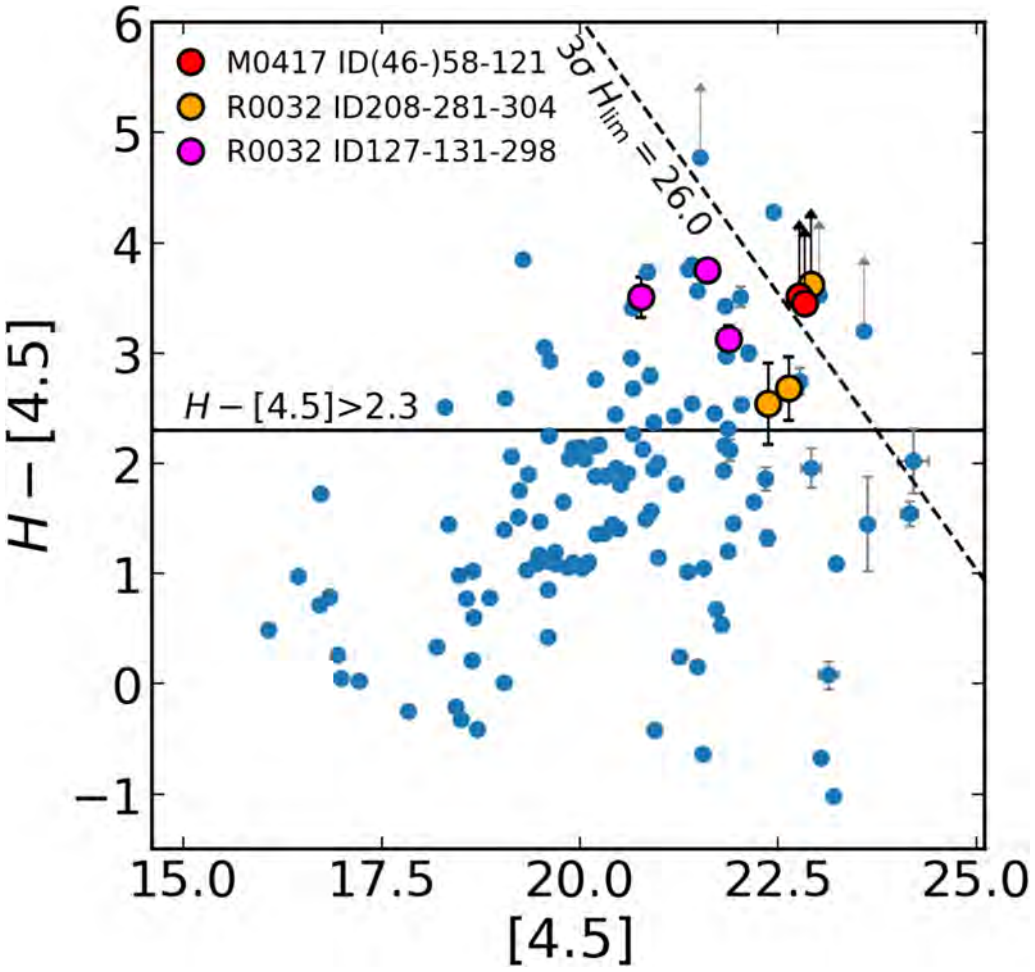

Figure 1. Color–magnitude diagram of ALCS sources. The black solid line represents the threshold of $H - [4.5] = 2.3$. The dashed line shows the location of $H = 26.0$ mag, which corresponds to the 3σ limit of the shallowest HST data in 33 ALCS cluster fields. The red, orange, and magenta dots represent three triply lensed images of our targets. However, M0417 ID46 is excluded due to contamination from a nearby bright source. For the *H*-dropout or HST-dark objects, the $H - [4.5]$ values are 3σ lower limits, as indicated by the arrows.

aperture with some aperture corrections centered on ALMA Band 6 continuum positions (V. Kokorev et al. 2022). To mitigate contamination from nearby sources, we use the residual IRAC maps, wherein sources detected in the HST maps are modeled with the IRAC PSF and subtracted.

From these NIR-dark objects, we focused on three triply lensed systems: ID46, ID58, and ID121 in the MACS J0417.5-1154 (hereafter M0417) cluster region; ID127, ID131, and ID198 in the RXC J0032.1+1808 (hereafter R0032) cluster region; and ID208, ID281, and ID304 in the R0032 cluster region. Figure 3 shows the multiband images for these sources. For clarity, we will hereafter refer to the three intrinsic sources as M0417-z365, R0032-z239, and R0032-z299, and their associated triply lensed images as M0417-z365.ID46/.ID58/.ID121, R0032-z239.ID127/.ID131/.ID198, and R0032-z299.ID208/.ID281/.ID304, respectively. The "z" values represent the spectroscopic redshift of each source, as described in Section 3.1. Note that M0417-z365.ID46 is excluded in Figure 1 due to the blending with a foreground galaxy (see Figure 3). These systems were predicted to be multiple images by our fiducial lens model (Section 3.2). Figure 2 shows their ALMA 1.2 mm continuum and HST images with critical lines of our fiducial lens models. We selected them since we are able to estimate their redshifts by the lens model, which allowed us to carry out line scan observations even though the photometric redshifts are unreliable.

2.4. ALMA Follow-up Line Scan Observations

Based on the redshift estimates, we conducted follow-up line scan observations for the three lensed systems with ALMA bands 3 and 4 (project code: 2019.1.00949.S and 2021.1.01246 for M0417 and R0032 region, respectively). Four and three different tunings were assigned to band 3 and 4 observations, respectively. The observational parameters are summarized in Table 1.

The fields of view of the observations are shown in Figure 2. The data were calibrated and flagged in the standard manner using the Common Astronomy Software Applications package (`CASA`; CASA Team et al. 2022). The four tunings for band 3 and the three tunings for band 4 were separately combined to create individual continuum images for each band using the `CASA/tclean` task with the natural weighting. The spectral channels where the emission line is detected were not used for the continuum imaging. Each tuning data was also imaged to produce a cube with a channel width of 40 MHz ($\sim$100 km s^{-1}) to search for emission lines after the continuum subtraction with `CASA/uvcontsub` task. The emission is cleaned down to the 2σ level. For all images and cube data, the

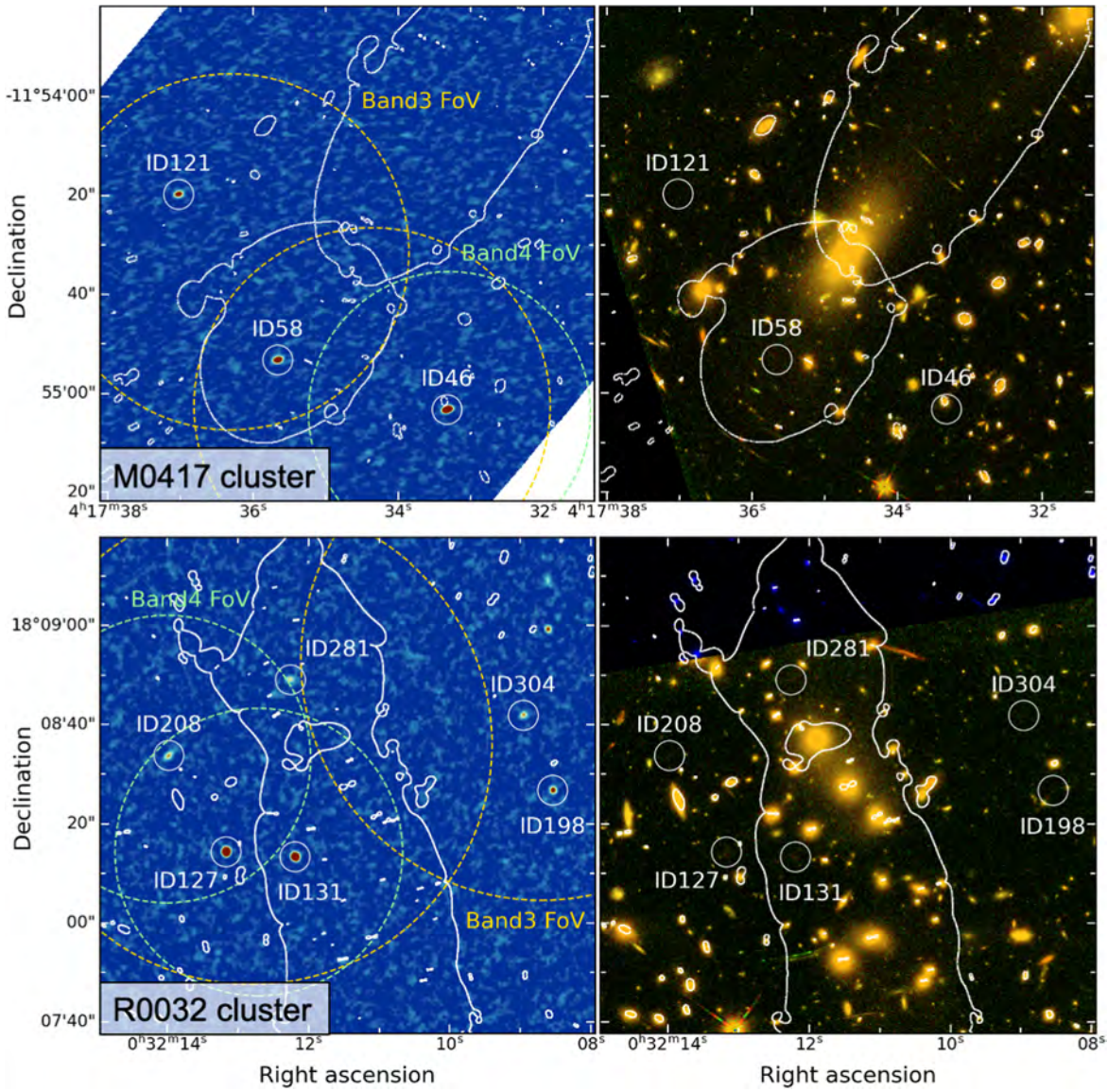

Figure 2. (Left) ALMA 1.2 mm continuum image of M0417 cluster. (Right) False-color HST image of M0417 cluster (red: F160W, green: F125W, blue: F814W). The top row shows the M0417 cluster and the bottom row shows the R0032 cluster. The white circles indicate the positions of multiple images of the NIR-dark galaxies. The white solid lines denote the critical lines of our fiducial lens model at $z = 3.652$ and 2.985 for M0417 and R0032, respectively. The yellow and green dashed lines represent the FoV of ALMA band 3 and 4 follow-up observations described in Section 2.4, respectively.

Table 1
ALMA Band 3 and 4 Observation Parameters

Project Code	Band	Target	Date	Antenna[a]	PWV (mm)	Frequency Range (GHz)	Beam Size	Cont. Sensitivity (μJy beam^{-1})
	3	M0417-z365.ID46/.ID58/.ID121	2019/12	C43-2	4.9–6.8	85.05–112.18	$3\farcs84 \times 2\farcs95$	4.6
2019.1.00949.S		(2-pointing mosaic)		(46–48)		(T1–T4)		
(PI: K. Kohno)	4	M0417-z365.ID46	2019/12	C43-1/2	2.5–3.3	130.57–153.95[b]	$2\farcs66 \times 1\farcs96$	7.6
		(1-pointing)		(42–43)		(T5–T7)		
	3	R0032-z239.ID127/.ID131/.ID198	2021/12	C43-4/5	1.5–7.5	85.06–112.18	$1\farcs04 \times 0\farcs87$	3.8
		R0032-z299.ID208/.ID281/.ID304	~2022/1	(41–45)		(T1–T4)		
2021.1.01246.S		(2-pointing mosaic)						
(PI: K. Kohno)	4	R0032-z239.ID127/.ID131	2022/8	C43-5	0.3–0.9	130.56–153.94[b]	$0\farcs77 \times 0\farcs53$	6.8
		R0032-z299.ID208		(44–47)		(T5–T7)		
		(2-pointing mosaic)						

Notes.
[a] Antenna configuration (the number in parentheses indicates the number of antennas).
[b] There is a frequency gap of about 2.75 GHz in this range as shown in Figure 4.

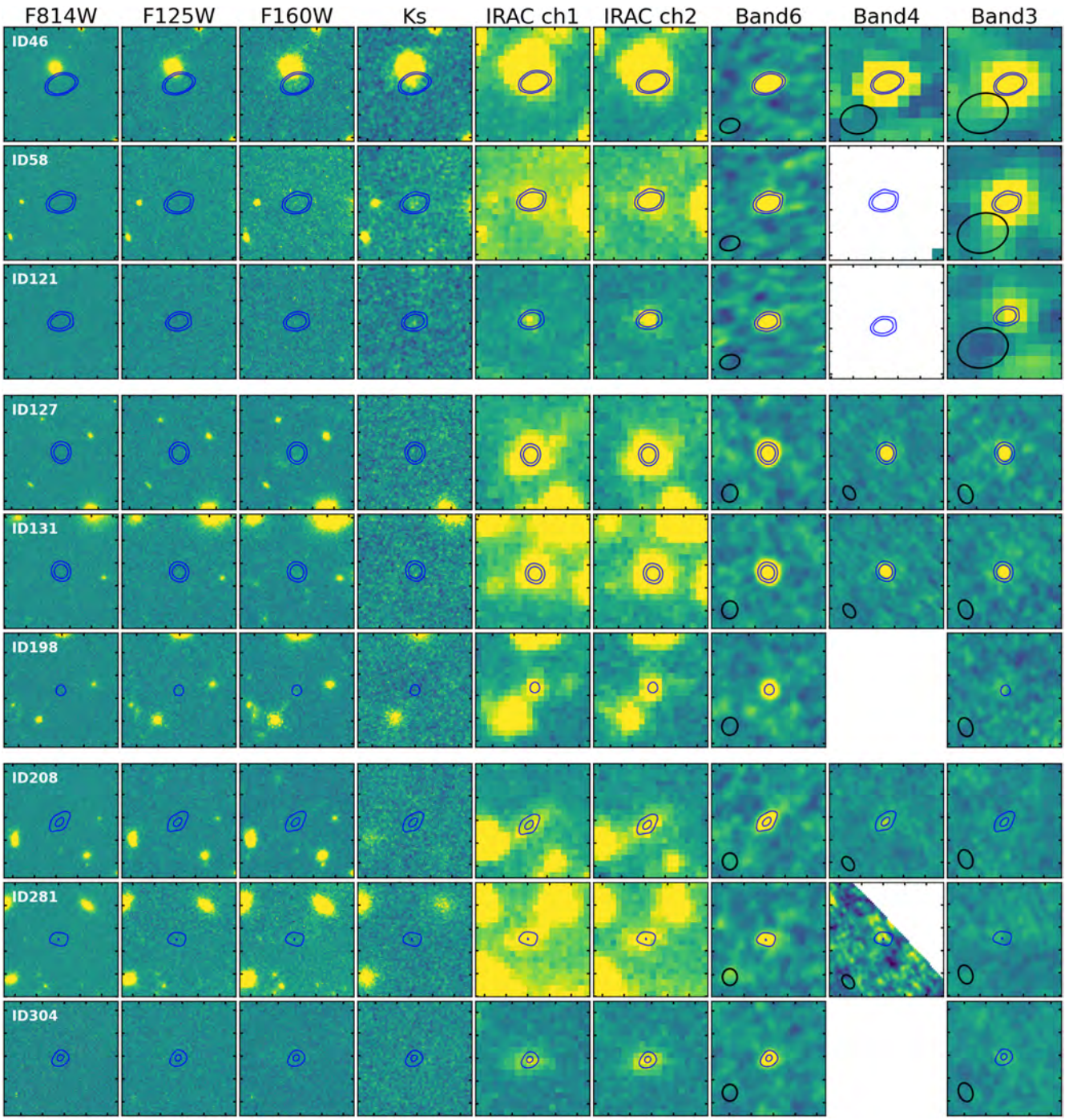

Figure 3. Multiband images for the three triply lensed systems. The blue contours denote the ALMA band 6 (1.2 mm) continuum drawn at [4, 8] $\times \sigma$ levels. The color scale is adjusted to show the 5σ range for each emission. The image size is $10'' \times 10''$. The black ellipses show the beam size.

primary beam correction is applied. We create images and cubes with a pixel size of $1''$ for both band 3 and 4 in the M0417. In the R0032 region, a pixel size of $0''.2$ is used for both Bands 3 and 4.

2.5. JCMT SCUBA-2 450 and 850 μm

We observed the M0417 cluster region at 450 μm and 850 μm with James Clerk Maxwell Telescope (JCMT)/ Submillimetre Common-User Bolometer Array 2 (SCUBA-2) (Program ID: M20AP036, PI: K. Kohno). Observations were conducted on 2020 February 4 and 16 and July 8 and 31 using the CV Daisy scan, which creates a $\sim 6'$ diameter circular map with a deep and uniform exposure coverage in the central $\sim 1.'5$ diameter region. The total on-source time was 7.2 hr under excellent weather conditions, where the measured atmospheric opacities at 225 GHz were less than 0.05. The typical beam sizes are $7''$ and $15''$ at 450 μm and 850 μm, respectively.

We reduced the data using the Dynamic Iterative Map Maker (DIMM) within the STARLINK Sub-Millimetre User Reduction Facility (SMURF) software package (E. Chapin et al. 2013). The maps for each individual exposure were

coadded and combined, using the STARLINK Pipeline for Combining and Analyzing Reduced Data (PICARD), and beam-match filtered. The resulting 1σ noise levels were $\sim$3.9 mJy and $\sim$0.6 mJy at 450 μm and 850 μm bands, respectively. The ALMA observations conducted by the ALCS did not detect any contamination sources near the positions of M0417-z365.ID46, ID58, and ID121. Therefore, no deblending was required, and the peak values at the ALMA Band 6 continuum positions were extracted as the source photometries.

2.6. K_S-band

In order to obtain better constraints on the stellar properties of faint ALMA sources without any counterpart in *H*-band, we observed M0417 cluster region at 2.16 μm *Ks*-band with the 6.5 m Magellan Baade Telescope/FourStar near-Infrared Camera on 2021 November 20 (PI: Wei-Hao Wang). We expect a significantly improved characterization of the stellar population (i.e., stellar mass, stellar age, visual extinction, etc.) by catching the 4000 Å break between *H*- and K_S-bands at $z \sim 3.7$ (the redshift of the triple-lensed images in the M0417 region, as we will conclude in Section 3.1). We obtained approximately 4.8 hr of on-source exposure. The final averaged seeing measured with PSFEx software is $\sim$0.″64. We extracted photometries using a $D = 1.''5$ aperture centered on the ALMA band 6 continuum positions for our target sources. We confirmed that this aperture maximizes the SNR of the enclosed flux density by drawing a growth curve. The noise level is obtained by 1000 random apertures on the sigma-clipped map. We note that the values in the weight map do not deviate significantly from the average at the source location. The aperture correction factor, calculated with the obtained PSF, is $\sim$1.4. The 5σ depth is measured to be 24.18 mag with the $D = 1.''5$ aperture.

For the R0032 region, we make use of K_S-band imaging data taken with the High Acuity Wide field *K*-band Imager (HAWK-I) on the Very Large Telescope. The *Ks*-band imaging of R0032 region (Program ID: 0103.A-0871(B), PI: A. Edge) is publicly available on the ESO Science archive. The final averaged seeing is $\sim$1.″12, and the 5σ depth is 22.81 mag with a $D = 2.''0$ aperture. No significant detection is obtained for our sources.

3. Data Analysis

3.1. Spectroscopic Redshift Identifications

3.1.1. M0417-z365.ID46/.ID58/.ID121

Due to the sufficiently large beam size, the detection can be considered as a point source. We first created integrated-intensity maps around 99.1 GHz for Band 3 and around 148.6 GHz for Band 4, where bright emission lines were detected. On these maps, we selected the pixels with peak values at each position of the triply lensed image. The spectra were then extracted from the cube image data at these specific pixels.

Emission lines are clearly detected at 99.114 $\pm$ 0.005 GHz with peak flux densities of 8.6σ, 7.3σ, and 5.4σ from ID46, 58, and 121, respectively. Here, the noise level is calculated as the standard deviation of the line-free channel fluxes at the same pixels, specifically those within 50 channels of the emission line, with an absolute flux calibration error of 5%.

Table 2
Velocity-integrated Line Flux Density

M0417-z365.	ID46	ID58	ID121	Total
μ	$5.1^{+2.6}_{-2.6}$	$3.9^{+1.6}_{-1.6}$	$3.4^{+1.4}_{-1.4}$	$12.5^{+3.3}_{-3.3}$
CO(4–3)	0.88 ± 0.06	0.59 ± 0.05	0.48 ± 0.05	1.95 ± 0.10
[C I](1–0)	0.16 ± 0.06	0.17 ± 0.06	0.16 ± 0.07	0.49 ± 0.11
CO(6–5)	1.20 ± 0.05	⋯	⋯	1.20 ± 0.05
R0032-z239.	ID127	ID131	ID198	Total
μ	$6.9^{+3.6}_{-3.5}$	$5.3^{+2.7}_{-2.7}$	$2.5^{+1.1}_{-1.0}$	$14.7^{+4.6}_{-4.6}$
CO(3–2)	3.5 ± 0.3	3.7 ± 0.3	1.1 ± 0.3	8.3 ± 0.5
CO(4–3)	5.9 ± 0.3	4.8 ± 0.4	⋯	10.7 ± 0.5
[C I](1–0)	3.7 ± 0.4	2.2 ± 0.5	⋯	5.9 ± 0.6
R0032-z299.	ID208	ID281	ID304	Total
μ	$7.9^{+4.1}_{-4.0}$	$4.3^{+1.8}_{-1.8}$	$3.0^{+1.3}_{-1.2}$	$15.2^{+4.6}_{-4.6}$
CO(3–2)	0.57 ± 0.17	0.42 ± 0.15	0.59 ± 0.13	1.6 ± 0.2
CO(5–4)	1.6 ± 0.3	⋯	⋯	1.6 ± 0.3

Note. μ is the magnification factor. The velocity-integrated line flux density is in units of Jy km s^{-1}. The magnification factor is not corrected.

We fitted the emission line with a single Gaussian and calculated the total flux as the integral over a frequency range of 1.5 × FWHM. For a more robust measurement, the FWHM of all lines is fixed to that of the CO(4–3) line with the highest SNR. The total fluxes are 14.6σ, 12.5σ, and 8.9σ from ID46, 58, and 121, respectively. This line detection confirms the initial prediction from our lens model that these three sources are triply lensed images. In addition, a bright emission line is detected at 148.650 $\pm$ 0.006 GHz from ID46 with a peak (total) flux = $9.6\sigma(22.3\sigma)$. The noise level of the total flux is calculated by summing, in quadrature, the rms noise from each channel derived from signal-free regions of the map across the channels containing the line. Furthermore, when combining the spectra of the triply lensed images, a faint emission line is marginally detected at 105.84 $\pm$ 0.02 GHz with a total flux of 4.6σ, although the peak flux density is only 3.4σ. We search the redshift solution that matches the three detected line combinations using a publicly available code[47] (T. J. L. C. Bakx & H. Dannerbauer 2022). Since the frequency spacing between CO rotational transition lines is constant, detecting two CO lines can result in multiple possible redshift solutions. This code visually identifies the correct redshift solution by considering the observed frequencies, as well as the presence of detected lines and the absence of others. The only solution is at $z = 3.6517 \pm 0.0002$ and the three lines are CO(4–3), [C I](1–0), and CO(6–5). This result is somewhat lower than the initial prediction from our lens model, $z = 4.5 \pm 0.5$. Figure 4 shows the full ALMA band-3/4 spectra for the three triply lensed NIR-dark sources, including the other two triply lensed images in the R0032 region discussed below. The line properties are summarized in Table 2. We similarly measured the band 3 and 4 continuum fluxes by extracting peak values near the source positions.

[47] https://github.com/tjlcbakx/redshift-search-graphs

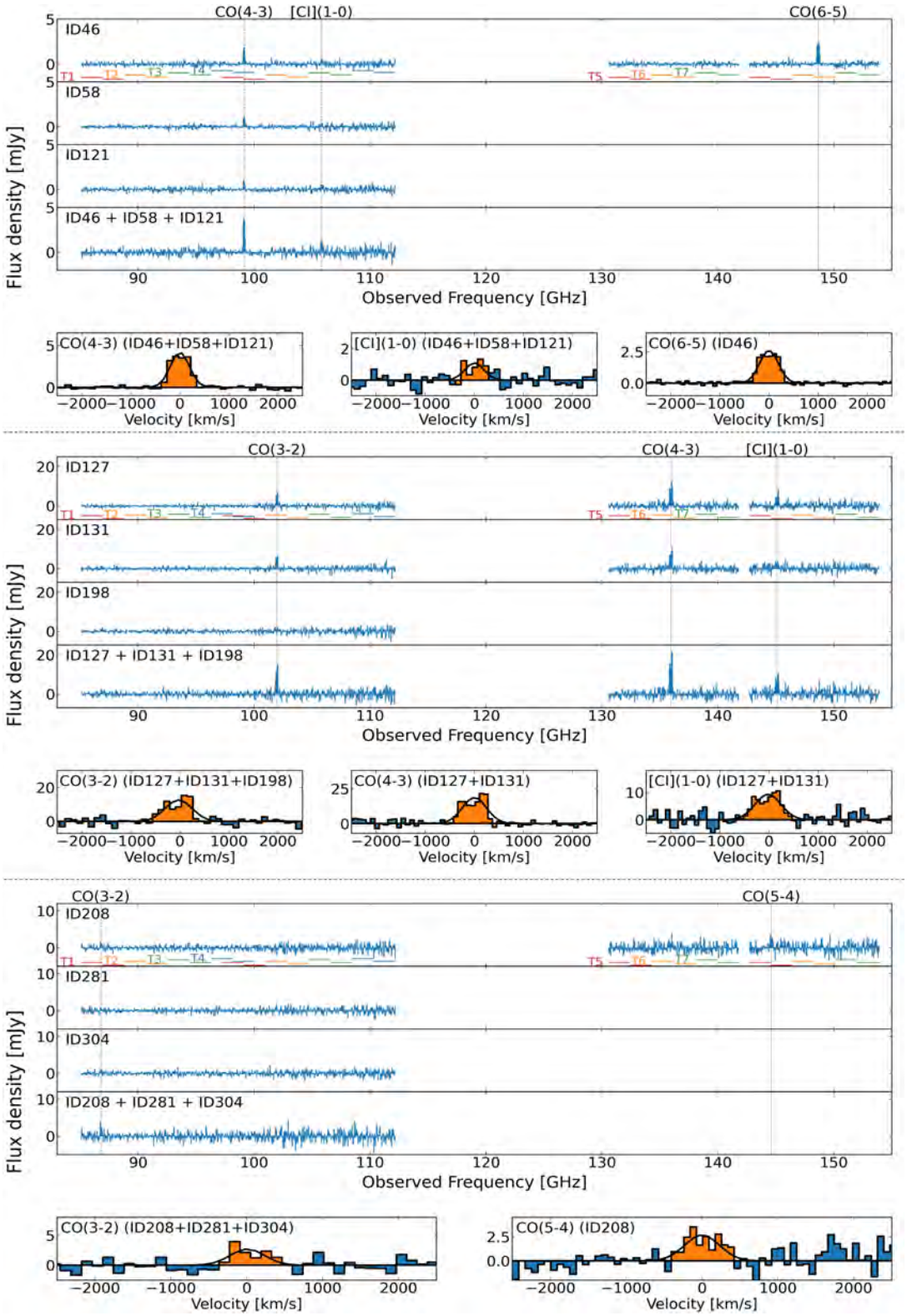

Figure 4. The obtained spectra from ALMA line scan observations toward M0417 ID46, 58, and 121 (top); R0032 ID127, 131, and 198 (middle); and R0032 ID208, 281, and 304 (bottom). For each triply lensed system, the top panel shows the full band-3/4 spectra from seven 7.5 GHz-wide independent tunings (T1–T7). The combined spectrum is also shown. The horizontal bars show the coverage of the seven tunings, each of which has four spectral windows. The positions of the identified emission lines are shown with vertical black dashed lines. In the bottom panel, enlarged views of combined line spectra are shown. Velocities are relative to $z = 3.652$, 2.391, and 2.985, respectively. The black solid lines are the best-fit single Gaussian. The orange shade indicates the integration range for the velocity-integrated flux.

3.1.2. R0032-z239.ID127/.ID131/.ID198

We used a circular aperture with a diameter of $D = 4''$ centered on the ALCS band 6 continuum positions to extract spectra and continuum fluxes. By drawing a growth curve, we confirmed that this aperture is sufficient to include source fluxes. Emission lines are clearly detected at 101.963 ± 0.008 GHz with peak (total) fluxes of $8.8\sigma(13.6\sigma)$, 6.9σ (11.7σ), and $2.5\sigma(3.3\sigma)$ from ID127, 131, and 198, respectively. Thus, these three sources are triply lensed images as predicted from our lens model. The total line fluxes are measured in the same manner as in Section 3.1.1. In addition, bright emission lines are detected at 135.956 ± 0.008 GHz and 145.123 ± 0.018 GHz from ID127 and ID131. From these lines, we conclude that this triply lensed source is at $z = 2.39112 \pm 0.00019$ and detected emission lines are CO(3–2), CO(4–3), and [C I](1–0). This result is consistent with the initial prediction from our lens model, $z = 2.0 \pm 0.5$.

3.1.3. R0032-z299.ID208/.ID281/.ID304

We reconstructed the initial lens model of the R0032 cluster with the additional constraint that the R0032-z239.ID127/.ID131/.ID198 are triply lensed images and then found that it is highly likely that the R0032-z299.ID208/.ID281/.ID304 are also triply lensed images. The spectra and continuum fluxes are measured in the same manner as in Section 3.1.2. An emission line is barely detected at 144.56 ± 0.03 GHz with peak (total) fluxes of $3.0\sigma(5.2\sigma)$ from ID208. In addition, when combining the spectra of the triply lensed images, a faint emission line is detected at 86.77 ± 0.02 GHz with a peak (total) flux of $5.1\sigma(6.2\sigma)$. These results conclude that this lensed source is at $z = 2.9853 \pm 0.0009$ and detected emission lines are CO(3–2) and CO(5–4). This result is consistent with the initial prediction from our lens model, $z = 3.0 \pm 0.5$. These consistencies enhance the reliability of the identified spectroscopic redshift, even though the line detections are marginal. We emphasize that the detection of the CO(3–2) line was made possible by the total magnification factor of $\sim$15, making the observation more than 100 times more efficient in terms of observation time.

3.2. Mass Model

We utilize the publicly available `glafic` code (M. Oguri 2010, 2021) to construct our fiducial lens models, following R. Kawamata et al. (2016) and T. Okabe et al. (2020). The multiple images that constrain the lens model are sourced from G. Mahler et al. (2019) for the M0417 cluster and from A. Acebron et al. (2020) for the R0032 cluster. Additionally, the three triply lensed systems identified in this study are included to provide further constraints. To assess the statistical uncertainty of the magnification factor, we employ a Markov Chain Monte Carlo (MCMC) method, taking into account uncertainties in the positions of the multiple images ($\Delta x = \Delta y = 0\farcs4$) and photometric redshifts ($\Delta z = 0.6$). The median value is chosen as the representative value, with the 16th and 84th percentiles serving as the uncertainty range. To account for potential systematic errors in the lens model, we introduce an additional error based on a comparison with other lens models that are constructed with different software, as detailed by S. Fujimoto et al. (2024). Specifically, we incorporate an error of 40% for magnifications below 5% and 50% for those above 5. The obtained magnification factors can be found in Table 2.

3.3. SED Fitting

We use the `CIGALE` code (M. Boquien et al. 2019) to perform SED fitting and estimate key physical parameters. The photometries used for the SED fitting are listed in Table 3. `CIGALE` models the SED panchromatically based on an energy balance principle, where all the absorbed energy is then reemitted by the dust in the mid/far-infrared domains. Following S. Huang et al. (2023b), instead of the default fixed grid parameter search in `CIGALE`, we implement a Bayesian-based approach using the `DYNESTY` package (J. S. Speagle 2020). This allows for efficient exploration of extensive parameter spaces and computation of the Bayesian posterior distribution for the free parameters. We use flat prior distributions for all parameters.

We assume a nonparametric star formation history (SFH; J. Leja et al. 2019) and adopt the stellar population model from G. Bruzual & S. Charlot (2003) with solar metallicity. The dust attenuation law is taken from D. Calzetti et al. (2000). For the dust infrared emission model, we use B. T. Draine et al. (2014) templates. We note that bright optical emission lines such as Hα and $[\mathrm{O\,III}]_{5007}$ do not fall into the photometric bands used for our sources at their redshifts. For each multiple image, we performed SED fitting and, based on the posterior distribution, determined the median value as the best-fit parameter, accompanied by the 16%–84% credible interval. In our case, differential magnification is negligible, meaning that the physical quantities scale linearly with the magnification factor. Therefore, the intrinsic physical quantities are derived by dividing the obtained apparent physical quantities by the magnification factor. After correcting each value for magnification, we took the intrinsic physical quantity as the average weighted by the inverse square of the uncertainties. The best-fit SED models along with their 16%–84% credible interval are shown in Figure 10. The obtained intrinsic physical parameters along with their 16%–84% credible interval are listed in Table 4. For the fiducial SFR value, we take one that is averaged over 100 Myr. The SFR can also be estimated from the total infrared luminosity ($L_{\rm IR}$) using the relation $\mathrm{SFR} = 4.5 \times 10^{-44}\,M_\odot\,\mathrm{yr}^{-1}\,(\mathrm{erg\,s}^{-1})^{-1}\,L_{\rm IR}$, which is a calibration by P. Madau & M. Dickinson (2014), but we multiply a factor of 0.63 to account for the correction from the Salpeter IMF to the Chabrier IMF. Using this equation, the SFR values inferred from $L_{\rm IR}$ are $167^{+63}_{-69}\,M_\odot\,\mathrm{yr}^{-1}$ for M0417-z365, $92^{+35}_{-35}\,M_\odot\,\mathrm{yr}^{-1}$ for R0032-z239, and $33^{+12}_{-16}\,M_\odot\,\mathrm{yr}^{-1}$ for R0032-z299. These values are consistent within the uncertainties with the SFRs derived from the SED fitting.

Figure 5 shows the SFR versus M_* relation of our three intrinsic sources. For comparison, JWST/NIRCam (long-wavelength filter)-selected H-band dropouts (3σ depth of $H > 27$mag, L. Barrufet et al. 2023), ALMA and Spitzer/IRAC-detected H-band dropouts (typical 5σ depth of $H > 27$ mag, T. Wang et al. 2019), $2 < z < 4$ SMGs from the AS2UDS samples (U. Dudzevičiūtė et al. 2020), NIR-dark SMGs (C. M. Casey et al. 2019; C. C. Williams et al. 2019; D. A. Riechers et al. 2020; H. Umehata et al. 2020; L. Zhou et al. 2020; S. M. Manning et al. 2022; V. Kokorev et al. 2023; I. Smail et al. 2023; F. Sun et al. 2024), and NIR-dark DSFGs (Y. Fudamoto et al. 2021) are also shown. Some of these previous studies estimate physical quantities using `MAGPHYS`

Table 3
Photometries of the Three NIR-dark Triply Lensed Systems (the Magnification Factor Is Not Corrected)

			M0417-z365			R0032-z239			R0032-z299			
Band	Wavelength	Unit	ID46	ID58	ID121	ID127	ID131	ID198	ID208	ID281	ID304	References
HST-F606W	606 nm	nJy	blended	<26	<26	<53	<53	<53	<53	<53	<53	K22
HST-F814W	814 nm	nJy	blended	<68	<68	<63	<63	<63	<63	<63	<63	K22
HST-F105W	1.05 μm	nJy	blended	<106	<106	<83	<83	<83	<83	<83	<83	K22
HST-F125W	1.25 μm	nJy	blended	<135	<135	<137	<137	<137	<137	<137	<137	K22
HST-F140W	1.40 μm	nJy	blended	<116	<116	207 ± 31	<119	<119	<119	<119	<119	K22
HST-F160W	1.60 μm	nJy	blended	<111	<111	262 ± 23	707 ± 121	362 ± 42	<88	<88	<88	K22
FourStar-*Ks*	2.2 μm	μJy	blended	0.85 ± 0.22	<0.63	⋯	⋯	⋯	⋯	⋯	⋯	This work
HAWKI-*Ks*	2.2 μm	μJy	⋯	⋯	⋯	<2.4	<2.4	<2.4	<2.4	<2.4	<2.4	This work
IRAC-ch1	3.6 μm	μJy	blended	1.59 ± 0.08	1.33 ± 0.07	4.77 ± 0.19	11.5 ± 0.2	3.77 ± 0.15	2.02 ± 0.19	2.5 ± 0.2	2.65 ± 0.16	K22
IRAC-ch2	4.5 μm	μJy	blended	2.85 ± 0.14	2.67 ± 0.14	8.32 ± 0.17	17.85 ± 0.17	6.44 ± 0.14	3.22 ± 0.17	2.5 ± 0.3	4.10 ± 0.14	K22
SPIRE	250 μm	mJy	45.4 ± 5.8	11.1 ± 7.3	10.9 ± 6.3	13.2 ± 5.3	12.7 ± 5.3	33.8 ± 7.7	<15.6	<15.7	⋯	S22
SPIRE	350 μm	mJy	39.0 ± 6.2	14.8 ± 5.3	6.9 ± 4.7	30.2 ± 7.4	15.6 ± 7.4	24.9 ± 8.4	<21.7	<21.8	<27.0	S22
SCUBA-2	450 μm	mJy	24.9 ± 4.0	14.3 ± 4.0	13.8 ± 3.8	⋯	⋯	⋯	⋯	⋯	⋯	This work
SPIRE	500 μm	mJy	30.7 ± 5.1	11.1 ± 5.7	17.6 ± 5.2	<38.9	32.7 ± 11.4	<23.0	10.6 ± 8.8	<21.8	<22.7	S22
SCUBA-2	850 μm	mJy	11.09 ± 0.65	5.4 ± 0.66	5.28 ± 0.65	⋯	⋯	⋯	⋯	⋯	⋯	This work
ALMA-B6	1.2 mm	mJy	4.3 ± 0.5	3.1 ± 0.4	2.1 ± 0.3	4.5 ± 0.5	3.9 ± 0.4	1.4 ± 0.2	1.2 ± 0.2	1.2 ± 0.2	1.1 ± 0.2	This work
ALMA-B4	2.1 mm	mJy	0.395 ± 0.018	⋯	⋯	1.1 ± 0.1	0.88 ± 0.09	⋯	0.41 ± 0.08	⋯	⋯	This work
ALMA-B3	3.0 mm	mJy	0.095 ± 0.007	0.051 ± 0.005	0.039 ± 0.007	0.25 ± 0.04	0.23 ± 0.04	<0.09	<0.08	<0.08	0.09 ± 0.03	This work

Table 4
Derived Intrinsic Physical Properties for Our Three Samples

Parameters		M0417-z365	R0032-z239	R0032-z299
Redshift	z	3.6517 ± 0.0002	2.3911 ± 0.0002	2.9853 ± 0.0009
Stellar mass	$\log_{10}(M_*/M_\odot)$	$10.37^{+0.23}_{-0.47}$	$10.04^{+0.20}_{-0.30}$	$9.82^{+0.19}_{-0.37}$
Infrared luminosity	$\log_{10}(L_{\rm IR}/L_\odot)$	$12.19^{+0.14}_{-0.15}$	$11.93^{+0.14}_{-0.14}$	$11.48^{+0.14}_{-0.17}$
Star formation rate (averaged over 100 Myr)	SFR $[M_\odot\ {\rm yr}^{-1}]$	101^{+39}_{-54}	52^{+18}_{-24}	21^{+8}_{-10}
Dust attenuation	A_V [mag]	$4.5^{+0.4}_{-0.4}$	$4.6^{+0.19}_{-0.20}$	$4.0^{+0.4}_{-0.5}$
Dust mass	$\log_{10}(M_{\rm dust}/M_\odot)$	$8.46^{+0.14}_{-0.14}$	$8.73^{+0.14}_{-0.15}$	$8.29^{+0.14}_{-0.14}$
Offset from the main sequence	ΔMS	$1.4^{+0.5}_{-0.7}$	$2.4^{+1.1}_{-0.8}$	$1.3^{+0.5}_{-0.6}$
Molecular gas mass (CO-based, $\alpha_{\rm CO}=1$)	$\log_{10}(M_{\rm gas}^{\rm CO)}/M_\odot)$	9.83 ± 0.14	10.22 ± 0.15	9.66 ± 0.16
Molecular gas mass ([C I]-based)	$\log_{10}(M_{\rm gas}^{\rm [C\,I])}/M_\odot)$	9.92 ± 0.15	10.71 ± 0.17	⋯
Gas depletion time ($\alpha_{\rm CO}=1$)	$\tau_{\rm gas}$ [Gyr]	$0.07^{+0.02}_{-0.03}$	$0.35^{+0.09}_{-0.14}$	$0.22^{+0.07}_{-0.10}$
Gas fraction ($\alpha_{\rm CO}=1$)	$f_{\rm gas}\equiv M_{\rm gas}/M_*$	$0.30^{+0.15}_{-0.32}$	$1.7^{+0.7}_{-1.1}$	$0.7^{+0.3}_{-0.6}$
1.2 mm continuum circularized radius	$R_{\rm e,1.2\ mm}$ [kpc]	$0.60^{+0.14}_{-0.24}$	$0.53^{+0.06}_{-0.14}$	$1.3^{+0.3}_{-0.3}$
Apparent axis ratio	b/a	$0.50^{+0.27}_{-0.32}$	$0.24^{+0.04}_{-0.07}$	$0.17^{+0.11}_{-0.07}$

(E. da Cunha et al. 2015). Different SED fitting codes often produce systematic differences in results due to various assumptions they employ, especially the dust attenuation models. R. Uematsu et al. (2024) investigated whether there are systematic differences in physical quantities obtained with MAGPHYS and CIGALE with the Calzetti attenuation curve, using the ALCS sample. They found that while the SFR estimates agree well, the stellar mass estimates from CIGALE are 0.37 dex lower at $M_* = 10^{10.5}\,M_\odot$. In any case, our sample remains significantly lower in SFR and stellar mass compared to the SMGs in previous studies. Our three samples lie on the main sequence (offset from the main sequence $\Delta{\rm MS} = {\rm SFR}/{\rm SFR_{MS}}$ is within a factor of 3), exhibiting a M_*–SFR relation similar to typical star-forming galaxies selected in NIR bands (e.g., C. Schreiber et al. 2015; C. M. S. Straatman et al. 2016). T. Wang et al. (2019) and M. Y. Xiao et al. (2023) suggest that such dust-obscured galaxies on the main sequence are a dominant population of the massive galaxies ($M_* \gtrsim 10^{9.5}\,M_\odot$) at $3 < z < 6$. Among our samples, M0417-z365 is located at a region where H-dropouts of T. Wang et al. (2019) are sampled. R0032-z299 is positioned on the lower mass and SFR region, bridging the gap with the dust-obscured galaxy candidates recently explored by JWST.

3.4. Molecular Gas Properties

We estimate the total molecular gas mass $M_{\rm gas}$ using the CO(3–2) line for the R0032-z239 and R0032-z299 and CO(4–3) line for the M0417-z365, respectively. We assume an average CO excitation of $r_{32/10} = 0.58 \pm 0.10$ and $r_{43/10} = 0.30 \pm 0.08$ (L. A. Boogaard et al. 2020), where r represents brightness temperature ratio. The value of CO-to-H_2 conversion factor $\alpha_{\rm CO}$ depends on various properties including metallicity, galactic environment, and morphology. In the following, we will show both results obtained with the assumption of $\alpha_{\rm CO} = 3.6\,M_\odot({\rm K\ km\ s^{-1}\ pc^2})^{-1}$, which is often assumed for massive MS galaxies (e.g., M. Aravena et al. 2019), and of $\alpha_{\rm CO} = 1.0\,M_\odot({\rm K\ km\ s^{-1}\ pc^2})^{-1}$, which is often assumed for SMGs and compact starbursts (e.g., M. S. Bothwell et al. 2013). We also calculate the molecular gas mass using [C I](1–0) luminosity for M0417-z365 and R0032-z239 following H. Umehata et al. (2020). The gas masses derived from both CO and [C I] luminosities are consistent provided that the $\alpha_{\rm CO}$ ranges between 1.0 and 3.6. We use CO-based molecular gas mass as a fiducial value. The gas depletion time $\tau_{\rm dep} = M_{\rm gas}/{\rm SFR}$ and gas fraction $f_{\rm gas} = M_{\rm gas}/M_*$ are also derived in conjunction with the SED fitting results. The obtained values are listed in Table 4.

The molecular gas depletion time ($\tau_{\rm dep} = M_{\rm gas}/{\rm SFR}$) and gas fraction ($f_{\rm gas} = M_{\rm gas}/M_*$) depend on redshift, stellar mass, and offset from the main sequence (ΔMS). L. J. Tacconi et al. (2018) compiled molecular gas mass data of star-forming galaxies at $0 < z < 4$, covering a wide range of stellar mass and ΔMS and derived the scaling relations of $\tau_{\rm dep} \propto (1+z)^{-0.62} \times \Delta{\rm MS}^{-0.44} \times M_*^{0.09}$ and $f_{\rm gas} \propto (1+z)^{2.5} \times \Delta{\rm MS}^{0.52} \times M_*^{-0.36}$. Figure 6 shows $\tau_{\rm dep}$ and $f_{\rm gas}$ as a function of ΔMS, normalized using the scaling relations. For comparison, we also plot ASPECS DEFGs (M. Aravena et al. 2020), NIR-dark SMGs in the literature (C. C. Williams et al. 2019; D. A. Riechers et al. 2020; H. Umehata et al. 2020; F. Sun et al. 2024). The gas depletion time and gas fraction of R0032-z299 are consistent with the scaling relation regardless of $\alpha_{\rm CO}$ value. This suggests that this galaxy is a normal star-forming galaxy undergoing secular evolution. M0417-z365 seems to exhibit a shorter $\tau_{\rm dep}$ and a smaller $f_{\rm gas}$, deviating by 0.80 dex and 0.96 dex from the scaling relations, respectively, assuming $\alpha_{\rm CO} = 1.0$ (0.25 dex and 0.41 dex if $\alpha_{\rm CO} = 3.6$). For R0032-z239, these quantities are consistent with the scaling relation when $\alpha_{\rm CO}$ is close to 1. Examining our results with those of the previous literature suggests that the NIR-dark galaxy population has a wide range of molecular gas depletion time and gas fraction. We will further discuss the interpretations of the molecular gas properties in Section 4.

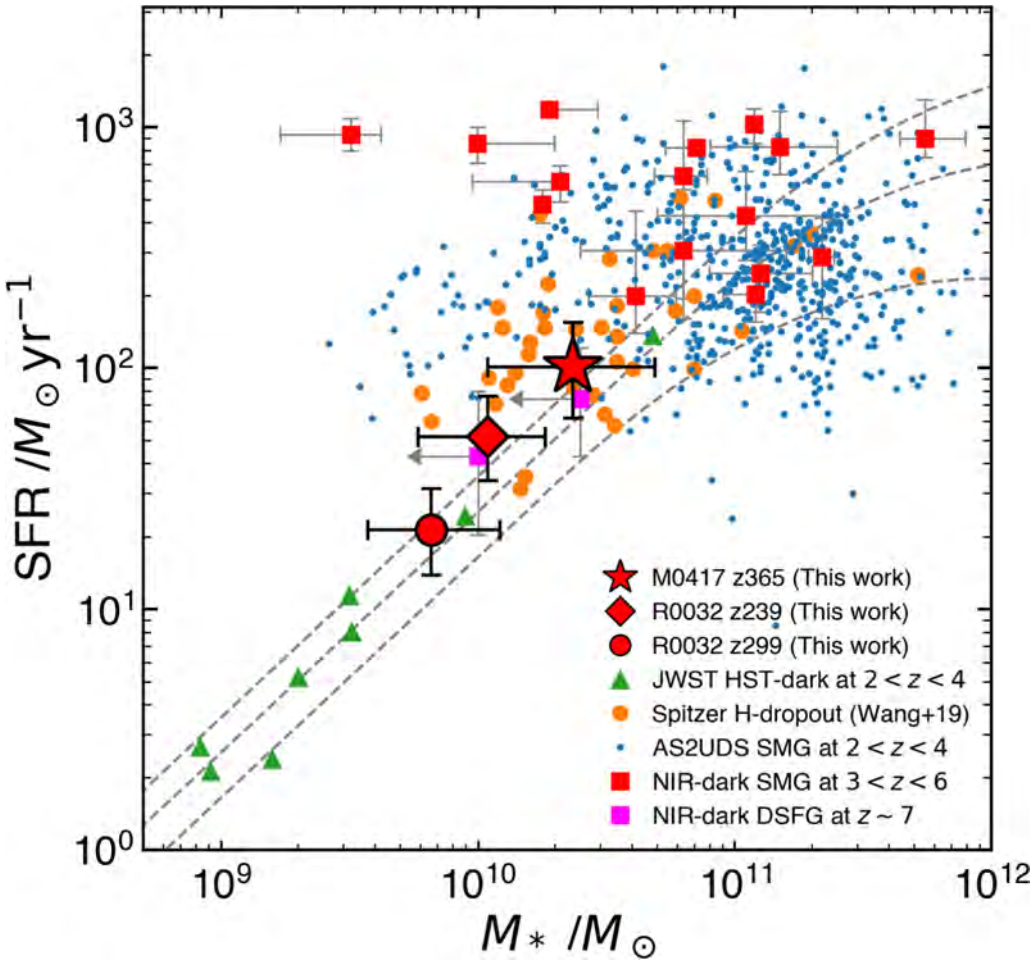

Figure 5. SFR against stellar mass relation for our three intrinsic sources (red star/diamond/circle) is shown along with other populations for comparison. The green triangle represents JWST/NIRCam selected *H*-dropouts at $2 < z < 4$ (L. Barrufet et al. 2023). The orange circle shows ALMA and Spitzer/IRAC-detected *H*-dropouts (T. Wang et al. 2019). The blue point represents $2 < z < 4$ SMGs from the AS2UDS samples (U. Dudzevičiūtė et al. 2020). The red squares are NIR-dark SMGs from the literature (C. M. Casey et al. 2019; C. C. Williams et al. 2019; D. A. Riechers et al. 2020; H. Umehata et al. 2020; L. Zhou et al. 2020; S. M. Manning et al. 2022; V. Kokorev et al. 2023; I. Smail et al. 2023; F. Sun et al. 2024). Two magenta squares are NIR-dark DSFGs at $z \sim 7$ (Y. Fudamoto et al. 2017). The gray dashed lines indicate the star-forming main sequence at $z = 3$, 4, and 5 (C. Schreiber et al. 2015).

Using the molecular gas masses derived above and the dust masses estimated from the SED fitting, we calculate the dust-to-gas mass ratio ($\delta_{\rm GDR} = M_{\rm dust}/M_{\rm gas}$). Assuming $\alpha_{\rm CO} = 1.0$, the dust-to-gas mass ratios based on CO luminosity are 23 ± 13 for M0417-z365, 31 ± 18 for R0032-z239, and 23 ± 14 for R0032-z299. When compared with the sample of SMGs at $z = 1$–5 presented in J. E. Birkin et al. (2021), where molecular gas masses are derived using CO with the assumption of $\alpha_{\rm CO} = 1.0$, the $\delta_{\rm GDR}$ values for our sources appear to be smaller, despite the large scatter in the sample. If the $\delta_{\rm GDR}$ of our sources is comparable to that of the $z = 1$–5 SMG sample, this could imply that $\alpha_{\rm CO}$ for our sources is larger than 1.0.

3.5. Morphology of the Star-forming Region

We reconstruct ALMA band 6 (1.2 mm) continuum images for the three triply lensed systems observed by ALCS using the `glafic` version 2. Ideally, it would be preferable to simultaneously fit the triply lensed images using a single source model. However, galaxy cluster lenses have complex gravitational potential such as small-scale substructures that are not accounted for in the parametric mass model. As a result, the positions of these multiple images typically often deviate by about $\sim 0\farcs5$ (e.g., M. Oguri et al. 2013). In this study, we perform individual fittings for each of the three images and then adopt their average value.

First, we refine the lens model by including the multiple images identified in this study as constraints, in addition to those previously recognized. Subsequently, we put a Sérsic source with a Sérsic index n of 1, characterized by six free parameters: *xy*-coordinates, flux, effective radius (half-light radius), major-to-minor axis ratio, and position angle) on the source plane and all source parameters are optimized with the lens parameters held constant. For χ^2 optimization, only the area within a 3″-radius circle centered on each source was considered.

The uncertainty in source reconstruction arises from both the lens model and the observed image. To address the uncertainty of the lens model, we utilize the multitude of lens models generated and accepted via the MCMC method when constructing the lens model as described in Section 3.2. We repeat the same `glafic` fitting process with these lens models. In addition, to consider the uncertainty of the observed image, we add a randomly generated noise map with the same noise level as the observed image to the best-fit (lensed) model image (which does not include noise; the image in the Model

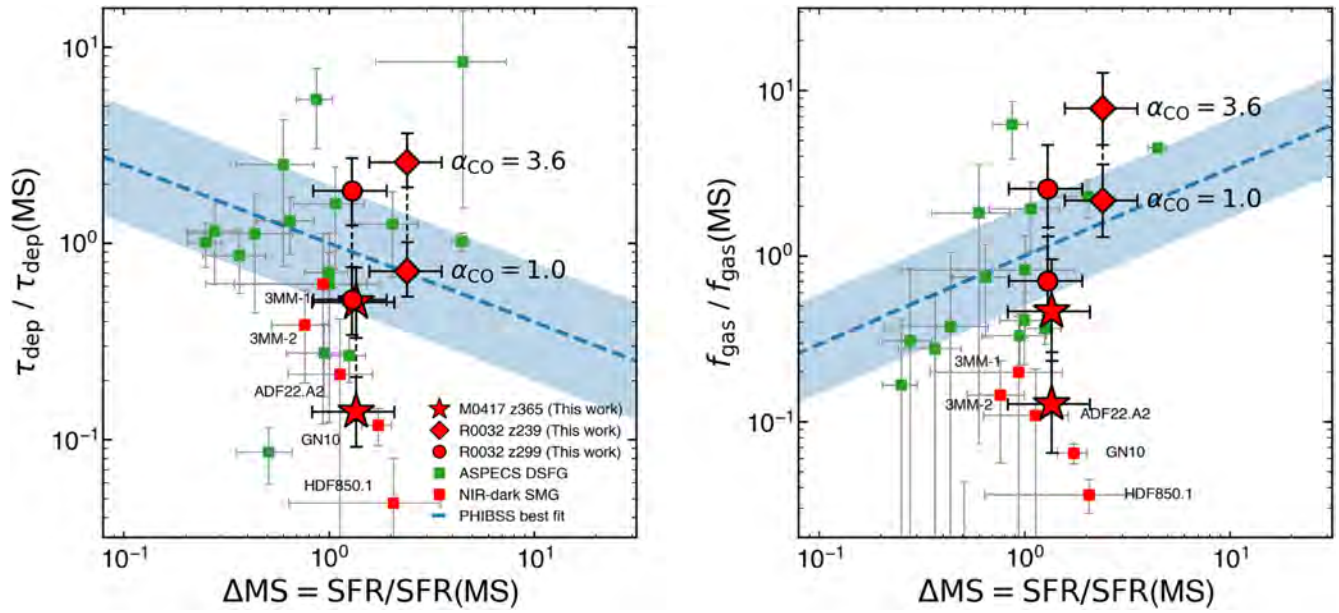

Figure 6. Gas depletion time against ΔMS (left) and gas fraction against ΔMS (right). The dashed line and blue shaded region show the best-fit line for the PHIBBS samples ($\tau_{gas}/\tau_{gas}(MS) = \Delta MS^{-0.40}$ and $f_{gas}/f_{gas}(MS) = \Delta MS^{0.53}$) derived in L. J. Tacconi et al. (2018) and its ±0.3 dex offset, respectively. The green square represents the ASPECS DSFG samples from M. Aravena et al. (2020), and the red square shows the NIR-dark SMGs for which gas mass is measured based on emission lines (C. C. Williams et al. 2019; D. A. Riechers et al. 2020; H. Umehata et al. 2020; F. Sun et al. 2024).

panel of Figure 7) and iterate the fitting. Given the pixel-correlated noise characteristic of interferometric images, we use a noise map convolved with the dirty beam of the ALMA observation. After conducting the fitting procedure 20,000 times in total, we adopt the median value as the best-fit value and use the 16%–84% interval as the uncertainty. In Appendix B, we further discuss the feasibility of spatially resolving the dust continuum from our ALMA observations.

Figure 7 shows the best-fit model for the three triply lensed systems. The obtained intrinsic circularized effective radius r_e and apparent axis ratio for them are listed in Table 4. Figure 8 shows the relation of the intrinsic infrared luminosities and circularized effective radii for our three samples along with massive ($10^{10.5}\,M_\odot < M_* < 10^{11}\,M_\odot$) MS SFGs at $z \sim 2$ (W. Rujopakarn et al. 2016), faint DSFGs with SFR of 10–100 $M_\odot/\mathrm{yr}^{-1}$ at $z = 1$–4 (J. González-López et al. 2017; N. Laporte et al. 2017; A. Pope et al. 2023; A. Mizener et al. 2024), massive ($M_* > 10^{11}\,M_\odot$) DSFGs at $z \sim 2$ (K. Tadaki et al. 2020), SCUBA-2 selected SMGs at $z = 1$–4 (B. Gullberg et al. 2019; U. Dudzevičiūtė et al. 2020), and NIR-dark SMGs (H. Umehata et al. 2017, 2020; C. Gómez-Guijarro et al. 2022). While the infrared luminosity of M0417-z365 and R0032-z239 is much lower than that of SMGs, their dust-emitting regions are as compact as those of NIR-dark SMGs. The tendency for compact objects to experience stronger dust attenuation has been suggested by other studies (e.g., I. Smail et al. 2021; C. Gómez-Guijarro et al. 2023). On the other hand, R0032-z299, the faintest one in our sample, has a more extended dust continuum of $R_{e,1.2\,mm} = 1.3 \pm 0.3$ kpc. The infrared surface densities of M0417-z365, R0032-z239, and R0032-z299 are $6.6^{+7.8}_{-3.3} \times 10^{11}$, $4.7^{+2.9}_{-1.9} \times 10^{11}$, and $2.8^{+2.6}_{-1.3} \times 10^{10}\,L_\odot\,\mathrm{kpc}^{-2}$, respectively. We will further discuss the interpretations of the size–luminosity relation in Section 4.

3.6. PDR Properties

The photodissociation regions (PDRs) play a dominant role in the heating, cooling, ionization, and dissociation of molecules in the neutral interstellar medium (ISM; A. G. G. M. Tielens & D. Hollenbach 1985; E. L. O. Bakes & A. G. G. M. Tielens 1994). The heating occurs when far-UV photons penetrate the ISM and are absorbed by polycyclic aromatic hydrocarbons (PAHs). These particles release photoelectrons, which collisionally excite the gas, ultimately converting the energy into dust emission. The gas cooling occurs primarily through FIR fine structure lines, such as [C II]$_1$58, [O I]$_6$3, and [C I] where the cooling rate depends on the gas density. Thus, we can constrain the gas density n_H and far-UV incident radiation field U_{UV} in PDRs from the dust luminosity (8 μm < λ < 1000 μm) and the ratio of CO to [C I] luminosity. We perform the PDR modeling for our two samples, M0417-z365 and R0032-z239, which have both CO(4–3) and [C I](1–0) line data using the `PDRTToolbox` (M. W. Pound & M. G. Wolfire 2008, 2011, 2023). The model of M. J. Kaufman et al. (2006) with the gas metallicity of $Z = 1$ and simple plane-parallel geometry is assumed.

Figure 9 shows the model predictions for $L_{[C\,I](1-0)}/L_{CO(4-3)}$ against $L_{[C\,I](1-0)}/L_{IR}$ together with the observed data of our two samples, previously reported NIR-dark SMGs at $z = 3.99$ (H. Umehata et al. 2020) and $z = 4.26$ (I. Smail et al. 2023), $z \sim 1$–5 bright SMGs (M. S. Bothwell et al. 2017; F. Valentino et al. 2020; K. C. Harrington et al. 2021; M. Hagimoto et al. 2023), MS SFGs at $z \sim 1$ (F. Valentino et al. 2020), $z \sim 2$–6.5 QSOs (S. Alaghband-Zadeh et al. 2013; M. S. Bothwell et al. 2013), and local U/LIRGs (T. Michiyama et al. 2021). While dust continuum and [C I](1–0) emission are generally optically thin, low-J CO emission is optically thick. Thus, we increase the observed CO(4–3) luminosity by a factor of 2 to incorporate this effect. M0417-z365 has a lower [C I]/CO and [C I]/FIR luminosity ratio than R0032-z239 and is located closer to other SMGs than MSs or R0032-z239, indicating a higher gas density and stronger radiation field. However, we note that the actual

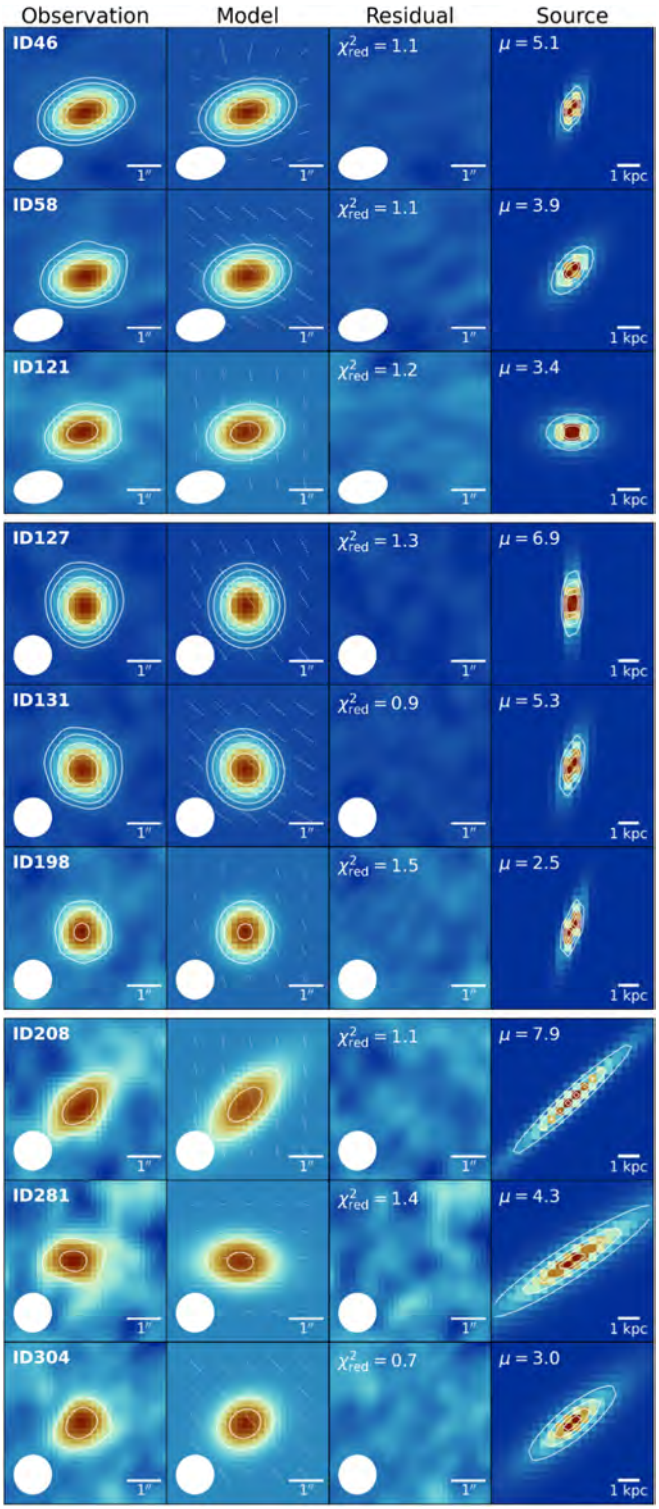

Figure 7. Source reconstruction for the three triply lensed systems. From left to right, the observed ALCS band 6 (1.2 mm) cleaned image, best-fit model, residual, and reconstructed source are shown. The white contours on the observed image and model image are drawn at [4, 8, 16, 32] × σ. The peak residuals are less than 3σ. The black contours in the source panel show 20%, 40%, 60%, and 80% of the peak. The synthesized beam size is displayed in the lower-left corner of each panel. The dotted line in the model panel shows the shear direction and strength at the position. The reduced chi-square values and magnification factors are annotated on the residual and source images, respectively.

ISM would consist of a range of molecular clouds that have different properties like density and radiation field rather than a simple plane-parallel model. Since our measurements are integrated over the whole galaxy, the obtained results should be treated qualitatively.

4. Discussion

In this section, we discuss how our three normal dust-obscured galaxies relate to the broader context of galaxy evolution, primarily based on the properties of molecular gas and the morphology of the star-forming regions.

4.1. M0417-z365 and R0032-z239: Compact Dust-obscured Galaxies

Both M0417-z365 and R0032-z239 are main sequence star-forming galaxies and they are characterized by having compact star-forming regions of ∼0.6 kpc, comparable to those of NIR-dark SMGs in the literature. The gas depletion time and molecular gas fraction of M0417-z365 seem to be lower than the scaling relation, although those gas properties are consistent with the scaling relation within the margin of error when $\alpha_{\rm CO}$ is 3.6. We first state an interpretation of the former case. D. Elbaz et al. (2018) and C. Gómez-Guijarro et al. (2022) focus on a galaxy population that lies on the MS but has gas depletion times shorter than the scaling relations like starburst (SB) galaxies. They term these galaxies "SBs in the MS" and report that they tend to have a smaller gas fraction and higher dust temperature (but see also S. Jin et al. 2019, 2022; M. Y. Xiao et al. 2023). Furthermore, the authors argue that the compactness of the dust continuum area correlates with these characteristics: As the star-forming region becomes more compact compared to the stellar disk, the gas depletion timescale and gas fraction become lower (see also E. F. Jiménez-Andrade et al. 2019). To phenomenologically explain this galaxy population, C. Gómez-Guijarro et al. (2022) propose a scenario in which the galaxy exhausts its gas from the outside and, through some mechanism, gradually becomes more compact. However, this is not confirmed observationally (L. Ciesla et al. 2023).

Next, we present an interpretation of the latter case. The molecular gas properties of R0032-z239 are also aligned with the scaling relation when $\alpha_{\rm CO}$ is close to 1. This case can be interpreted as being in a compaction phase of a steady galaxy evolution scenario for MS galaxies, proposed by cosmological simulations (e.g., A. Zolotov et al. 2015; S. Tacchella et al. 2016). In this scenario, the galaxy experiences compaction of gas and star formation triggered by an intense gas inflow event such as minor mergers or counter-rotating streams. This phase is then followed by inside-out quenching driven by outflows and central gas depletion. These processes are repeated until the halo mass grows sufficiently to halt cold gas accretion from the intergalactic medium. Throughout these cycles, the galaxy remains MS on the SFR–M_* plane and upholds the scaling relations for gas depletion time and gas fraction.

Both M0417-z365 and R0032-z239 have compact star-forming regions, which aligns with prior studies suggesting a correlation between compactness and the strength of dust attenuation (I. Smail et al. 2021). However, based only on our

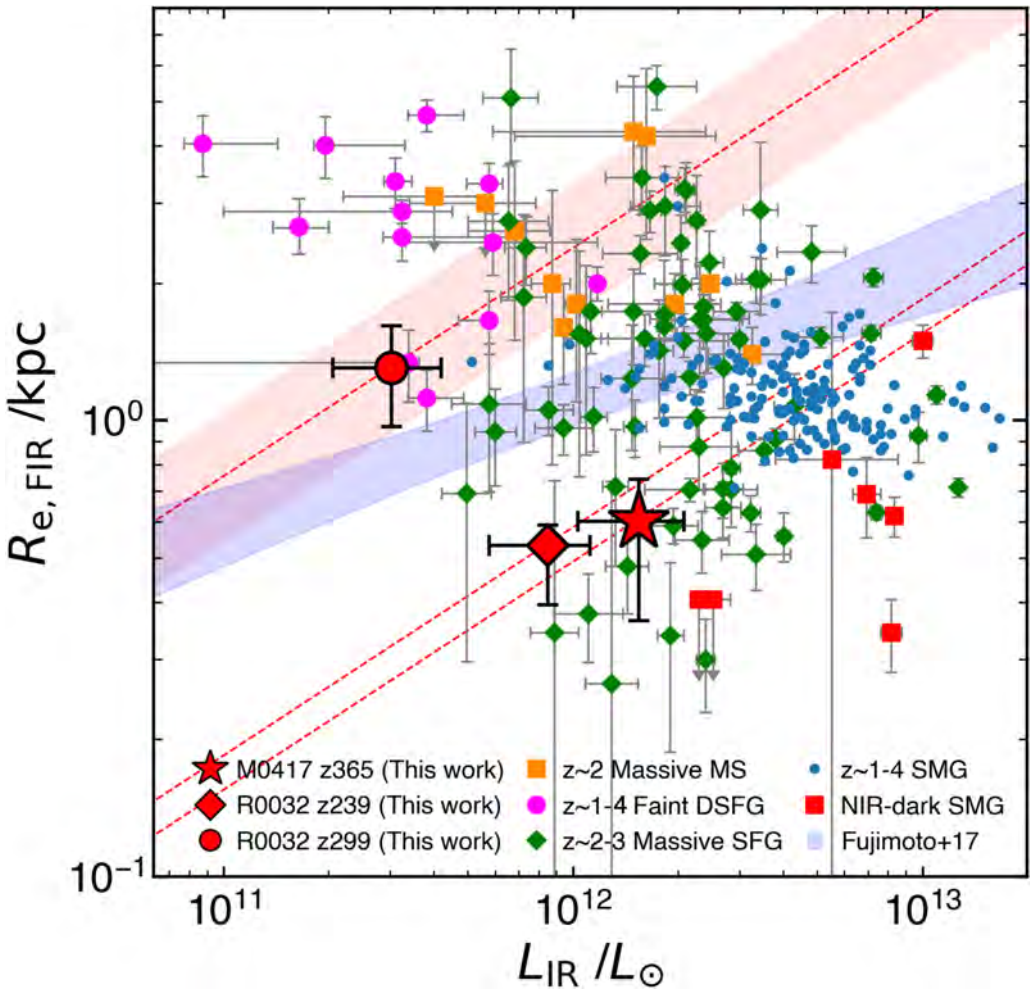

Figure 8. Intrinsic infrared luminosities vs. circularized effective radii for our three samples, massive main sequence galaxies at $z \sim 2$ (W. Rujopakarn et al. 2016), faint DSFGs at $z \sim 1$–4 (J. González-López et al. 2017; N. Laporte et al. 2017; A. Pope et al. 2023; A. Mizener et al. 2024), massive ($M_* > 10^{11}\,M_\odot$) SFGs at $z \sim 2$–3 (K. Tadaki et al. 2020), AS2UDS SMGs at $z = 1$–4 (B. Gullberg et al. 2019; U. Dudzevičiūtė et al. 2020; I. Smail et al. 2021), and NIR-dark SMGs (H. Umehata et al. 2017, 2020; C. Gómez-Guijarro et al. 2022). The red dashed lines (with a shaded region of 1σ uncertainty for R0032-z299) correspond to the constant infrared surface density relations for our samples. The blue shaded region shows the scaling relation with 1σ uncertainty derived from a statistical ALMA archival study (S. Fujimoto et al. 2017).

current results, it is unclear whether this compactness is the actual cause of the strong dust attenuation observed in these galaxies.

4.2. R0032-z299: A Normal DSFG with Edge-on Disk

R0032-z299, the faintest source in our sample, is an LIRG-class MS SFG and its gas depletion time and gas fraction are consistent with the scaling relation, which suggests that this galaxy is under secular evolution. This source has a dust continuum that is roughly twice as extended as the other two samples and NIR-dark SMGs in the literature. Its infrared surface brightness of $\Sigma_{IR} = 2.8^{+2.6}_{-1.3} \times 10^{10}\,L_\odot\,\mathrm{kpc}^{-2}$ is more than an order of magnitude lower. The FIR size–luminosity relation at $z \gtrsim 2$ is not well constrained at the faint end of $L_{IR} < 10^{12}\,L_\odot$. While S. Fujimoto et al. (2017) postulates in their statistical ALMA study that fainter galaxies tend to be smaller, J. González-López et al. (2017) and W. Rujopakarn et al. (2016) report that, despite large scatter, the FIR sizes of fainter DSFGs at $z \sim 1$–2 are either comparable to or exceed those of brighter SMGs. In the local universe, the IR–size relation has been investigated down to $L_{IR} \sim 10^{10}\,L_\odot$, suggesting that galaxies with lower L_{IR} tend to have larger sizes (J. McKinney et al. 2023b).

B. Gullberg et al. (2019) stack dust continuum of SCUBA-2 detected bright SMGs to find not only a central compact (subkiloparsec) component but also a fainter extended component extending about a few kiloparsecs associated with (unobscured) star and molecular gas. The infrared surface brightness of the compact and extended components are about (6–10) $\times\ 10^{11}$ and $1 \times 10^{10}\,L_\odot\,\mathrm{kpc}^{-2}$, respectively. As the SFR increases, the infrared surface brightness of the compact component shows a rising trend, while that of the extended component remains constant. Based on this result and simulation works (e.g., P. F. Hopkins et al. 2013), the authors argue that the two components are physically decoupled. They suggest that the compact component likely represents a merger-induced starburst triggered by radial gas inflow that loses its angular momentum. Meanwhile, the extended component seems to be a regular disk that had formed before the merger.

The infrared surface brightness of R0032-z299 is comparable to that of the extended component identified by B. Gullberg et al. (2019) and those of faint ($L_{IR} \lesssim 10^{12}\,L_\odot$)

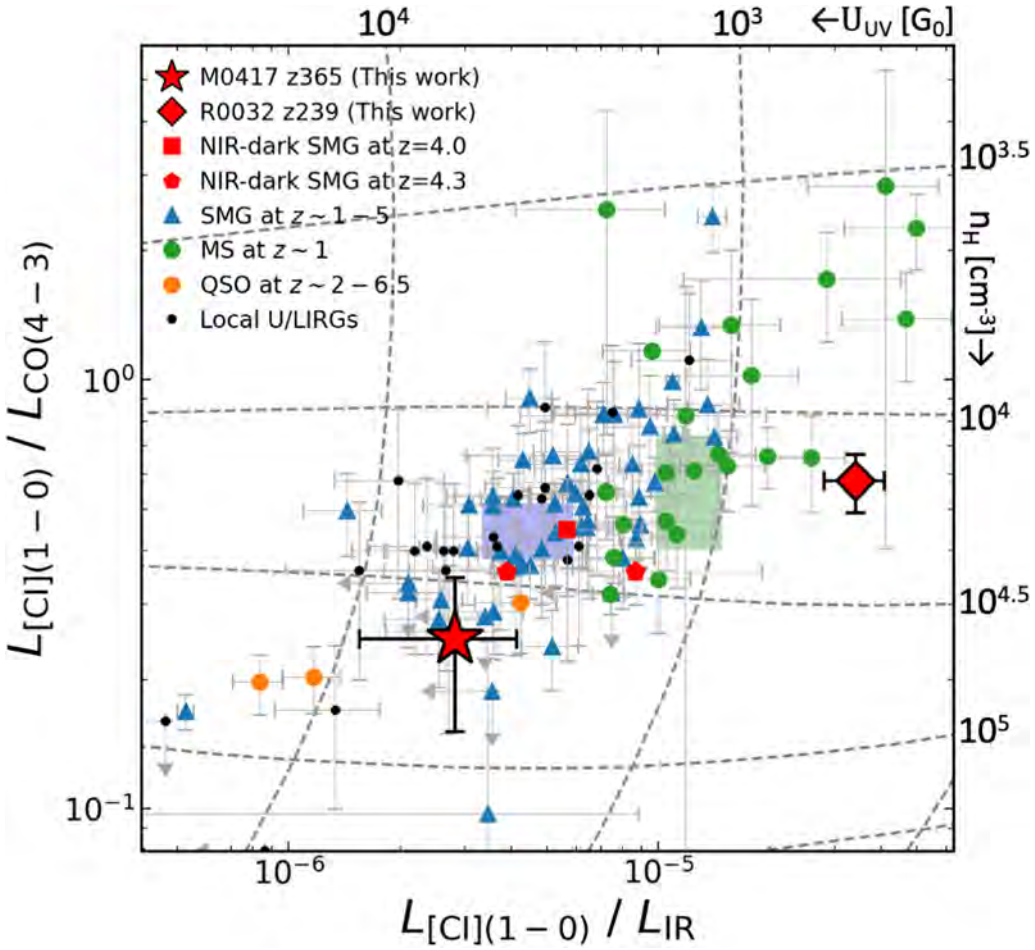

Figure 9. $L_{[C\,I](1-0)}/L_{CO(4-3)}$ against $L_{[C\,I](1-0)}/L_{IR}$ for model and observed values. The horizontal and vertical gray dashed lines represent the model tracks for constant n_H [cm^{-3}] and U_{UV} [G_0], respectively. $G_0 = 1.6 \times 10^{-3}$ ergs cm^{-2} s^{-1} is the far-UV radiation field in the vicinity of the Sun (H. J. Habing 1968). The red star and diamond are our two samples. The red square and pentagon show NIR-dark SMGs at $z = 3.99$ (H. Umehata et al. 2020) and $z = 4.26$ (I. Smail et al. 2023), respectively. The blue triangle denotes $z \sim 1$–5 bright SMGs (S. Alaghband-Zadeh et al. 2013; M. S. Bothwell et al. 2017; J. E. Birkin et al. 2021; K. C. Harrington et al. 2021; M. Hagimoto et al. 2023). The green and orange circles represent the MS SFGs at $z \sim 1$ (N. Bourne et al. 2019; F. Valentino et al. 2020) and $z \sim 2$–4 quasar (S. Alaghband-Zadeh et al. 2013; M. S. Bothwell et al. 2017). The black dot shows local U/LIRGs (T. Michiyama et al. 2021). The arrows indicate the 3σ upper limits. The green and blue shaded regions represent the mean line luminosity ratios of MS and SMGs with 2σ uncertainty derived in F. Valentino et al. (2020), respectively.

DSFGs (W. Rujopakarn et al. 2016; J. González-López et al. 2017). Together with the normal molecular gas properties, we interpret that R0032-z299 is in a secular evolution phase prior to an outside-in transformation caused by mergers or violent disk instability. Another characteristic of this source is its elongated projected axis ratio of 0.17, the most elongated of our three samples. If we assume axisymmetry, R0032-z299 is likely to be a dusty edge-on disk, although there is another case that even a face-on galaxy can appear elongated if we are viewing a bar-like structure (e.g., J. A. Hodge et al. 2019; S. Huang et al. 2023a). Nonetheless, to explain the origin of the strong dust attenuation ($A_V \sim 4$), we interpret that this galaxy has an extended dusty edge-on disk, which causes the stellar light to be strongly attenuated by the large dust column density (W. Wang et al. 2018). This interpretation suggests that even normal dusty star-forming galaxies can be strongly dust-obscured and missed in optical/NIR observations, depending on the orientation to the observer. Recently, a JWST study discovered an HST-dark galaxy population with similar properties to R0032-z299: massive ($M_* \gtrsim 10^{10}\,M_\odot$), extended ($R_{e,F444W} \sim 1$–2 kpc), and edge-on disk galaxies (E. J. Nelson et al. 2023). We think that these JWST/NIRCam selected HST-dark galaxies and R0032-z299 are the same population and that our ALMA observations directly capture the dust responsible for the attenuation. These were identified in the early observations of JWST, suggesting that such a galaxy population is not uncommon. The geometric orientation —whether a galaxy is observed from an edge-on angle or not —would not be the only factor of the strong dust attenuation (S. Fujimoto et al. 2023; C. Gómez-Guijarro et al. 2023; B. Lorenz et al. 2023), but in massive galaxies where a disk is present, the edge-on disk orientation may be a significant factor contributing to dust attenuation. However, it should be noted that a recent simulation study predicts that edge-on disks tend to have less dust attenuation because stellar light escapes from the edges of the dust distribution (R. Cochrane et al. 2024). In the near future, we expect that deep multiband observation with a high angular resolution by HST, JWST, and ALMA will statistically reveal the detailed properties of dust-obscured galaxies and the origins of strong dust attenuation by directly comparing the spatial distribution of stars and dust. It would also be important to break the degeneracy between dust mass and dust temperature by observing the dust continuum with multiple bands.

5. Summary

We present spectroscopic redshifts and physical characterizations of three triply lensed dust-obscured galaxies that were originally detected in the ALCS program. The multiple images are apparently bright at 1.2 mm band but intrinsically faint ($S_{1.2\,\mathrm{mm}} < 1$ mJy) compared with classical SMGs due to the lens magnifications.

We perform ALMA band 3/4 line scan follow-up observations and successfully confirm the spectroscopic redshifts to be $z = 3.6517$, 2.3911, and 2.9853 for M0417-z365, R0032-z239, and R0032-z299, respectively. We also conduct follow-up observations toward the triply lensed sources in M0417 with the SCUBA-2/450, 850 μm and FourStar/K-band to collect more multiband photometries. Together with archival HST, Spitzer/IRAC, Herschel/SPIRE, and VLT/HAWK-I data, the stellar masses, SFRs, and visual extinctions are derived from panchromatic SED fitting. Thanks to a total magnification factor of up to ∼15, we were able to detect faint CO emission lines and estimate the gas mass.

Our three samples are located in the MS region in the M_*–SFR plane, with lower M_* and SFR than classical SMGs. They show a variety in molecular gas depletion time, gas fraction, and spatial extent of dust. M0417-z365 and R0032-z239 have compact 1.2 mm dust size of ∼0.6 kpc, comparable to those of previously reported NIR-dark SMGs, following a proposed trend that the more compact the dust continuum size, the higher the A_V. On the other hand, the dust continuum of R0032-z299 is roughly twice as extended as the other two samples and NIR-dark SMGs in the literature. Its infrared surface brightness is more than an order of magnitude lower than the other two samples and SMGs, which suggests that R0032-z299 is a different population. The molecular gas depletion time and gas fraction of R0032-z299 are consistent with a scaling relation for star-forming galaxies, suggesting this galaxy undergoes a secular evolution phase. R0032-z299 has an elongated projected axis ratio of ∼0.17, the most elongated of our three samples. This suggests that the edge-on dusty disk configuration causes strong dust attenuation. If so, even normal DSFGs can be strongly dust-obscured and missed in optical/NIR observations, depending on the orientation to the observer.

Acknowledgments

We thank Masato Hagimoto for providing us with the [C I] (1–0)/CO(4–3)/FIR data. We appreciate Takeo Minezaki for constructive comments and suggestions. We also sincerely thank the anonymous referee for constructive comments and suggestions, which have improved the quality of this paper. This paper makes use of the following ALMA data: ADS/JAO.ALMA# 2018.1.00035.L, #2019.1.00949.S, and #2021.1.01246.S. ALMA is a partnership of ESO (representing its member states), NSF (USA), and NINS (Japan), together with NRC (Canada), NSTC and ASIAA (Taiwan), and KASI (Republic of Korea), in cooperation with the Republic of Chile. The Joint ALMA Observatory is operated by ESO, AUI/NRAO, and NAOJ. This work is based (in part) on data collected at the Magellan Telescopes, with the support from the ALTA program of ASIAA. Data analysis was in part carried out on the Multi-wavelength Data Analysis System operated by the Astronomy Data Center (ADC), NAOJ. This research was supported by FoPM, WINGS Program, the University of Tokyo. A.T. was supported by the ALMA Japan Research Grant of NAOJ ALMA Project, NAOJ-ALMA-343. A.T. also acknowledges the support by JSPS KAKENHI grant No. 24KJ0562. K.K. acknowledges the support by JSPS KAKENHI grant No. JP17H06130 and JP22H04939, and the NAOJ ALMA Scientific Research grant No. 2017-06B. H.U. appreciates the support by JSPS KAKENHI grant No. 20H01953, 22KK0231, and 23K20240. W.H.W. and Z.K.G. acknowledge support by NSTC grant 111-2112-M-001-052-MY3. F.S. acknowledges JWST/NIRCam contract to the University of Arizona NAS5-02015. R.U. appreciates the support by JSPS KAKENHI grant No. 22J22795. F.E.B. acknowledges support from ANID-Chile BASAL CATA FB210003, FONDECYT Regular 1200495, and Millennium Science Initiative Program—ICN12_009.

Facilities: HST (ACS and WFC3), Magellan:Baade (FourStar), VLT:Yepun (HAWK-I), Spitzer (IRAC), Herschel (PACS), JCMT (SCUBA-2), ALMA.

Software: Astropy (Astropy Collaboration et al. 2022), Glafic (M. Oguri 2010), CASA (J. P. McMullin et al. 2007), Photutils (L. Bradley et al. 2022), SExtractor (E. Bertin & S. Arnouts 1996), PSFEx (E. Bertin 2011), CIGALE (M. Boquien et al. 2019), PDRToolbox (M. W. Pound & M. G. Wolfire 2023), Dynesty (J. S. Speagle 2020).

Appendix A
SED Fitting

Table 5 lists the parameter ranges used for our SED fitting. Figure 10 shows the SED fit results for all our sources.

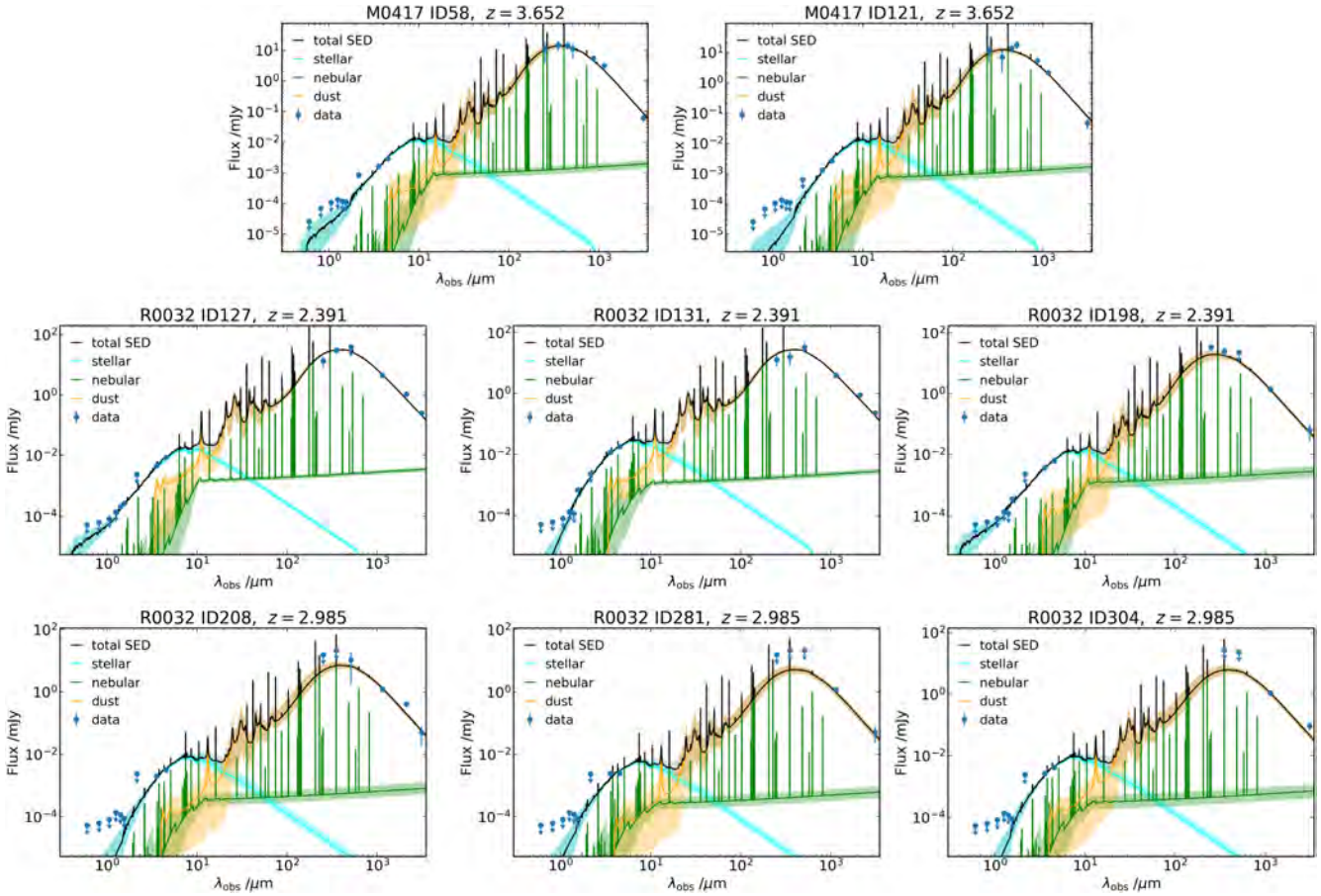

Figure 10. Median (solid lines) and 16th–84th percentile range (shaded regions) SEDs of our samples. The arrows indicate the 3σ flux upper limits used in the SED fitting.

Table 5
Parameter Ranges Used for the SED Fitting with CIGALE

Parameter	Symbol	Value
SFH (nonparametric; J. Leja et al. 2019)		
Number of constant SFH bins		6
Prior		Continuity ($SFR_n/SFR_{n+1} \sim$ Student's-t distribution)
SSP (bc03; G. Bruzual & S. Charlot 2003)		
Initial mass function	IMF	G. Chabrier (2003)
Metallicity of the stellar model	Z_{star}	0.02
Nebular emission (nebular)		
Ionization parameter	$\log U$	−2.0
Gas metallicity	Z_{gas}	0.02
Electron density	$n_e[cm^{-3}]$	100
Dust attenuation (dustatt_calzleit; D. Calzetti et al. 2000)		
Color excess of the stellar continuum light for the young population	$E(B-V)_*$	0–10
Reduction factor to apply $E(B-V)_*$ for the old population		0–1
UV bump amplitude		0
Slope of the power law modifying the attenuation curve	δ	−0.7–0.4
Dust emission (dl14; B. T. Draine et al. 2014)		
Mass fraction of polycyclic aromatic hydrocarbons (PAH)	q_{PAH}	0.47, 1.12, 2.50, 3.19, 3.90
Minimum radiation field	U_{min}	All possible values above 5.0
Power-law index of starlight intensity distribution	α	All possible values (1.0–3.0)
Fraction illuminated from U_{min} to U_{max}	$1-\gamma$	0–1

Note. We use flat prior distributions for all parameters. t_z represents the age of the universe at redshift z.

Appendix B
Intrinsic Dust Continuum Size

In Section 3.5, we reconstructed the intrinsic source morphology of the 1.2 mm continuum from ALCS observations using an MCMC approach. Here, we discuss an alternative method to demonstrate that the ALCS observations, with a resolution of $\sim 1''$, are capable of spatially resolving structures with $r_e \sim 0.5$ kpc.

In principle, it is possible to resolve sources smaller than the beam if the beam profile is well-defined, the SNR is sufficiently high, and some assumptions about the source light profile are made. J. M. Simpson et al. (2015) demonstrated that when the source size is close to the synthesized beam size and a peak SNR is more than ∼10, source sizes can be recovered with a precision of ∼30%. A. Tsujita et al. (2022) demonstrated that, in the presence of strong lensing, it is possible to measure source sizes even when they are smaller than the effective beam size. The minimum radius r_{min} that can be reliably measured can be expressed as follows (I. Martí-Vidal et al. 2012; C. Gómez-Guijarro et al. 2022): $r_{min} \simeq 0.44 \quad \theta_{beam}/\sqrt{SNR}$, where θ_{beam} is the FWHM of the beam. Note that the effective angular resolution is improved by a factor of $\sqrt{\mu}$ due to the strong lensing. For example, M0417-z365.ID46 has a magnification factor of $\mu = 5.1$ (Table 2) and a peak SNR of ∼50 (S. Fujimoto et al. 2024). Substituting these values into the above equation yields $r_{min} \sim 0.''03$, which corresponds to ∼0.2 kpc at $z = 3.652$. This calculation demonstrates that this source is indeed resolvable with our observations. Similarly, for M0417-z365.ID58 and M0417-z365.ID121, we obtain $r_{min} \sim 0.3$ kpc and ∼0.4 kpc at $z = 3.652$, respectively. For R0032-z239.ID127, R0032-z239.ID131, and R0032-z239.ID198, the calculations yield $r_{min} \sim 0.2$ kpc, ∼0.2 kpc, and ∼0.5 kpc at $z = 2.391$, respectively. Likewise, for R0032-z239.ID208, R0032-z239.ID281, and R0032-z239.ID304, we obtain $r_{min} \sim 0.4$ kpc, ∼0.5 kpc, and ∼0.6 kpc at $z = 2.985$. These results confirm that all sources in our sample are spatially resolved.

ORCID iDs

Akiyoshi Tsujita https://orcid.org/0000-0002-0498-5041
Kotaro Kohno https://orcid.org/0000-0002-4052-2394
Shuo Huang https://orcid.org/0009-0006-1731-6927
Masamune Oguri https://orcid.org/0000-0003-3484-399X
Ken-ichi Tadaki https://orcid.org/0000-0001-9728-8909
Ian Smail https://orcid.org/0000-0003-3037-257X
Hideki Umehata https://orcid.org/0000-0003-1937-0573
Zhen-Kai Gao https://orcid.org/0000-0003-1262-7719
Wei-Hao Wang https://orcid.org/0000-0003-2588-1265
Fengwu Sun https://orcid.org/0000-0002-4622-6617
Seiji Fujimoto https://orcid.org/0000-0001-7201-5066
Tao Wang https://orcid.org/0000-0002-2504-2421
Ryosuke Uematsu https://orcid.org/0000-0001-6653-779X
Daniel Espada https://orcid.org/0000-0002-8726-7685
Francesco Valentino https://orcid.org/0000-0001-6477-4011
Yiping Ao https://orcid.org/0000-0003-3139-2724
Franz E. Bauer https://orcid.org/0000-0002-8686-8737
Bunyo Hatsukade https://orcid.org/0000-0001-6469-8725
Fumi Egusa https://orcid.org/0000-0002-1639-1515
Yuri Nishimura https://orcid.org/0000-0003-0563-067X
Anton M. Koekemoer https://orcid.org/0000-0002-6610-2048
Daniel Schaerer https://orcid.org/0000-0001-7144-7182
Claudia Lagos https://orcid.org/0000-0003-3021-8564
Miroslava Dessauges-Zavadsky https://orcid.org/0000-0003-0348-2917
Gabriel Brammer https://orcid.org/0000-0003-2680-005X
Karina Caputi https://orcid.org/0000-0001-8183-1460
Eiichi Egami https://orcid.org/0000-0003-1344-9475
Jorge González-López https://orcid.org/0000-0003-3926-1411
Jean-Baptiste Jolly https://orcid.org/0000-0002-3405-5646
Kirsten K. Knudsen https://orcid.org/0000-0002-7821-8873
Vasily Kokorev https://orcid.org/0000-0002-5588-9156
Georgios E. Magdis https://orcid.org/0000-0002-4872-2294
Masami Ouchi https://orcid.org/0000-0002-1049-6658
Sune Toft https://orcid.org/0000-0003-3631-7176
John F. Wu https://orcid.org/0000-0002-5077-881X
Adi Zitrin https://orcid.org/0000-0002-0350-4488

References

Acebron, A., Zitrin, A., Coe, D., et al. 2020, ApJ, 898, 6
Alaghband-Zadeh, S., Chapman, S. C., Swinbank, A. M., et al. 2013, MNRAS, 435, 1493

Alcalde Pampliega, B., Pérez-González, P. G., Barro, G., et al. 2019, ApJ, 876, 135
Aravena, M., Boogaard, L., Gónzalez-López, J., et al. 2020, ApJ, 901, 79
Aravena, M., Decarli, R., Gónzalez-López, J., et al. 2019, ApJ, 882, 136
Astropy Collaboration, Price-Whelan, A. M., Lim, P. L., et al. 2022, ApJ, 935, 167
Bakes, E. L. O., & Tielens, A. G. G. M. 1994, ApJ, 427, 822
Bakx, T. J. L. C., & Dannerbauer, H. 2022, MNRAS, 515, 678
Barrufet, L., Oesch, P., Marques-Chaves, R., et al. 2025, MNRAS, 537, 3453
Barrufet, L., Oesch, P. A., Weibel, A., et al. 2023, MNRAS, 522, 449
Bertin, E. 2011, in ASP Conf. Ser. 442, Astronomical Data Analysis Software and Systems XX, ed. I. N. Evans et al. (San Francisco, CA: ASP), 435
Bertin, E., & Arnouts, S. 1996, A&AS, 117, 393
Birkin, J. E., Weiss, A., Wardlow, J. L., et al. 2021, MNRAS, 501, 3926
Boogaard, L. A., van der Werf, P., Weiss, A., et al. 2020, ApJ, 902, 109
Boquien, M., Burgarella, D., Roehlly, Y., et al. 2019, A&A, 622, A103
Bothwell, M. S., Aguirre, J. E., Aravena, M., et al. 2017, MNRAS, 466, 2825
Bothwell, M. S., Smail, I., Chapman, S. C., et al. 2013, MNRAS, 429, 3047
Bourne, N., Dunlop, J. S., Simpson, J. M., et al. 2019, MNRAS, 482, 3135
Bouwens, R. J., Illingworth, G. D., Oesch, P. A., et al. 2012, ApJ, 754, 83
Bradley, L., Sipőcz, B., Robitaille, T., et al. 2022, astropy/photutils: v1.10.0, Zenodo, doi:10.5281/zenodo.6825092
Bruzual, G., & Charlot, S. 2003, MNRAS, 344, 1000
Calzetti, D., Armus, L., Bohlin, R. C., et al. 2000, ApJ, 533, 682
Caputi, K. I., Dunlop, J. S., McLure, R. J., et al. 2012, ApJL, 750, L20
CASA Team, Bean, B., Bhatnagar, S., et al. 2022, PASP, 134, 114501
Casey, C. M., Zavala, J. A., Aravena, M., et al. 2019, ApJ, 887, 55
Chabrier, G. 2003, PASP, 115, 763
Chapin, E., Gibb, A. G., Jenness, T., et al. 2013, SMURF—The Sub-Millimetre User Reduction Facility Starlink User Note 258,
Ciesla, L., Gómez-Guijarro, C., Buat, V., et al. 2023, A&A, 672, A191
Cochrane, R., Anglés-Alcázar, D., Cullen, F., & Hayward, C. C. 2024, ApJ, 961, 37
Coe, D., Salmon, B., Bradač, M., et al. 2019, ApJ, 884, 85
da Cunha, E., Walter, F., Smail, I. R., et al. 2015, ApJ, 806, 110
Draine, B. T., Aniano, G., Krause, O., et al. 2014, ApJ, 780, 172
Dudzevičiūtė, U., Smail, I., Swinbank, A. M., et al. 2020, MNRAS, 494, 3828
Egami, E., Rex, M., Rawle, T. D., et al. 2010, A&A, 518, L12
Elbaz, D., Leiton, R., Nagar, N., et al. 2018, A&A, 616, A110
Franco, M., Elbaz, D., Béthermin, M., et al. 2018, A&A, 620, A152
Fudamoto, Y., Ivison, R. J., Oteo, I., et al. 2017, MNRAS, 472, 2028
Fudamoto, Y., Oesch, P. A., Schouws, S., et al. 2021, Natur, 597, 489
Fujimoto, S., Bezanson, R., Labbe, I., et al. 2023, arXiv:2309.07834
Fujimoto, S., Kohno, K., Ouchi, M., et al. 2024, ApJS, 275, 36
Fujimoto, S., Ouchi, M., Ono, Y., et al. 2016, ApJS, 222, 1
Fujimoto, S., Ouchi, M., Shibuya, T., & Nagai, H. 2017, ApJ, 850, 83
Gómez-Guijarro, C., Elbaz, D., Xiao, M., et al. 2022, A&A, 659, A196
Gómez-Guijarro, C., Magnelli, B., Elbaz, D., et al. 2023, A&A, 677, A34
González-López, J., Bauer, F. E., Romero-Cañizales, C., et al. 2017, A&A, 597, A41
Gruppioni, C., Béthermin, M., Loiacono, F., et al. 2020, A&A, 643, A8
Gullberg, B., Smail, I., Swinbank, A. M., et al. 2019, MNRAS, 490, 4956
Habing, H. J. 1968, BAN, 19, 421
Hagimoto, M., Bakx, T. J. L. C., Serjeant, S., et al. 2023, MNRAS, 521, 5508
Harrington, K. C., Weiss, A., Yun, M. S., et al. 2021, ApJ, 908, 95
Hatsukade, B., Ohta, K., Yabe, K., et al. 2015, ApJ, 810, 91
Hodge, J. A., & da Cunha, E. 2020, RSOS, 7, 200556
Hodge, J. A., Smail, I., Walter, F., et al. 2019, ApJ, 876, 130
Hopkins, P. F., Cox, T. J., Hernquist, L., et al. 2013, MNRAS, 430, 1901
Huang, S., Kawabe, R., Kohno, K., et al. 2023a, ApJL, 958, L26
Huang, S., Umehata, H., Kawabe, R., et al. 2023b, ApJ, 953, 75
Jiménez-Andrade, E. F., Magnelli, B., Karim, A., et al. 2019, A&A, 625, A114
Jin, S., Daddi, E., Magdis, G. E., et al. 2019, ApJ, 887, 144
Jin, S., Daddi, E., Magdis, G. E., et al. 2022, A&A, 665, A3
Kaufman, M. J., Wolfire, M. G., & Hollenbach, D. J. 2006, ApJ, 644, 283
Kawamata, R., Oguri, M., Ishigaki, M., Shimasaku, K., & Ouchi, M. 2016, ApJ, 819, 114
Kohno, K., Fujimoto, S., Tsujita, A., et al. 2023, Proc. of the 7th Chile-Cologne-Bonn Symp., Physics and Chemistry of Star Formation: The Dynamical ISM Across Time and Spatial Scales, ed. V. Ossenkopf-Okada et al. (Köln: Universitäts- und Stadtbibliothekj Köln), 16
Kokorev, V., Brammer, G., Fujimoto, S., et al. 2022, ApJS, 263, 38
Kokorev, V., Jin, S., Magdis, G. E., et al. 2023, ApJL, 945, L25
Lagos, C. d. P., da Cunha, E., Robotham, A. S. G., et al. 2020, MNRAS, 499, 1948
Laporte, N., Bauer, F. E., Troncoso-Iribarren, P., et al. 2017, A&A, 604, A132
Leja, J., Carnall, A. C., Johnson, B. D., Conroy, C., & Speagle, J. S. 2019, ApJ, 876, 3
Lorenz, B., Kriek, M., Shapley, A. E., et al. 2023, ApJ, 951, 29
Lotz, J. M., Koekemoer, A., Coe, D., et al. 2017, ApJ, 837, 97
Madau, P., & Dickinson, M. 2014, ARA&A, 52, 415
Mahler, G., Sharon, K., Fox, C., et al. 2019, ApJ, 873, 96
Manning, S. M., Casey, C. M., Zavala, J. A., et al. 2022, ApJ, 925, 23
Martí-Vidal, I., Pérez-Torres, M. A., & Lobanov, A. P. 2012, A&A, 541, A135
McKinney, J., Manning, S. M., Cooper, O. R., et al. 2023a, ApJ, 956, 72
McKinney, J., Pope, A., Kirkpatrick, A., et al. 2023b, ApJ, 955, 136
McMullin, J. P., Waters, B., Schiebel, D., Young, W., & Golap, K. 2007, in ASP Conf. Ser. 376, Astronomical Data Analysis Software and Systems XVI, ed. R. A. Shaw, F. Hill, & D. J. Bell (San Francisco, CA: ASP), 127
Michiyama, T., Saito, T., Tadaki, K.-i., et al. 2021, ApJS, 257, 28
Mizener, A., Pope, A., McKinney, J., et al. 2024, ApJ, 970, 30
Nelson, E. J., Suess, K. A., Bezanson, R., et al. 2023, ApJL, 948, L18
Oguri, M. 2010, PASJ, 62, 1017
Oguri, M. 2021, PASP, 133, 074504
Oguri, M., Schrabback, T., Jullo, E., et al. 2013, MNRAS, 429, 482
Okabe, T., Oguri, M., Peirani, S., et al. 2020, MNRAS, 496, 2591
Oke, J. B. 1974, ApJS, 27, 21
Pérez-González, P. G., Barro, G., Annunziatella, M., et al. 2023, ApJL, 946, L16
Pope, A., McKinney, J., Kamieneski, P., et al. 2023, ApJL, 951, L46
Pope, A., Montaña, A., Battisti, A., et al. 2017, ApJ, 838, 137
Postman, M., Coe, D., Benìtez, N., et al. 2012, ApJS, 199, 25
Pound, M. W., & Wolfire, M. G. 2008, in ASP Conf. Ser. 394, Astronomical Data Analysis Software and Systems XVII, ed. R. W. Argyle, P. S. Bunclark, & J. R. Lewis (San Francisco, CA: ASP), 654
Pound, M. W., & Wolfire, M. G., 2011 PDRT: Photo Dissociation Region Toolbox, Astrophysics Source Code Library, ascl:1102.022
Pound, M. W., & Wolfire, M. G. 2023, AJ, 165, 25
Riechers, D. A., Hodge, J. A., Pavesi, R., et al. 2020, ApJ, 895, 81
Romano, M., Cassata, P., Morselli, L., et al. 2020, MNRAS, 496, 875
Rujopakarn, W., Dunlop, J. S., Rieke, G. H., et al. 2016, ApJ, 833, 12
Salpeter, E. E. 1955, ApJ, 121, 161
Schreiber, C., Pannella, M., Elbaz, D., et al. 2015, A&A, 575, A74
Shu, X., Yang, L., Liu, D., et al. 2022, ApJ, 926, 155
Simpson, J. M., Smail, I., Swinbank, A. M., et al. 2015, ApJ, 799, 81
Simpson, J. M., Swinbank, A. M., Smail, I., et al. 2014, ApJ, 788, 125
Smail, I., Dudzevičiūtė, U., Gurwell, M., et al. 2023, ApJ, 958, 36
Smail, I., Dudzevičiūtė, U., Stach, S. M., et al. 2021, MNRAS, 502, 3426
Smail, I., Ivison, R. J., Kneib, J. P., et al. 1999, MNRAS, 308, 1061
Speagle, J. S. 2020, MNRAS, 493, 3132
Speagle, J. S., Steinhardt, C. L., Capak, P. L., & Silverman, J. D. 2014, ApJS, 214, 15
Straatman, C. M. S., Spitler, L. R., Quadri, R. F., et al. 2016, ApJ, 830, 51
Sun, F., Egami, E., Fujimoto, S., et al. 2022, ApJ, 932, 77
Sun, F., Egami, E., Pérez-González, P. G., et al. 2021, ApJ, 922, 114
Sun, F., Helton, J. M., Egami, E., et al. 2024, ApJ, 961, 69
Swinbank, A. M., Karim, A., Smail, I., et al. 2012, MNRAS, 427, 1066
Tacchella, S., Dekel, A., Carollo, C. M., et al. 2016, MNRAS, 457, 2790
Tacconi, L. J., Genzel, R., Saintonge, A., et al. 2018, ApJ, 853, 179
Tadaki, K., Iono, D., Yun, M. S., et al. 2020, ApJ, 889, 141
Tielens, A. G. G. M., & Hollenbach, D. 1985, ApJ, 291, 722
Tsujita, A., Tadaki, K.-i., Kohno, K., et al. 2022, PASJ, 74, 1429
Uematsu, R., Ueda, Y., Kohno, K., et al. 2024, ApJ, 965, 108
Umehata, H., Smail, I., Swinbank, A. M., et al. 2020, A&A, 640, L8
Umehata, H., Tamura, Y., Kohno, K., et al. 2017, ApJ, 835, 98
Valentino, F., Magdis, G. E., Daddi, E., et al. 2020, ApJ, 890, 24
Wang, T., Elbaz, D., Schreiber, C., et al. 2016, ApJ, 816, 84
Wang, T., Schreiber, C., Elbaz, D., et al. 2019, Natur, 572, 211
Wang, W., Kassin, S. A., Pacifici, C., et al. 2018, ApJ, 869, 161
Williams, C. C., Labbe, I., Spilker, J., et al. 2019, ApJ, 884, 154
Xiao, M., Oesch, P., Elbaz, D., et al. 2024, Natur, 635, 311
Xiao, M. Y., Elbaz, D., Gómez-Guijarro, C., et al. 2023, A&A, 672, A18
Yamaguchi, Y., Kohno, K., Hatsukade, B., et al. 2019, ApJ, 878, 73
Yamaguchi, Y., Tamura, Y., Kohno, K., et al. 2016, PASJ, 68, 82
Zavala, J. A., Casey, C. M., Manning, S. M., et al. 2021, ApJ, 909, 165
Zhou, L., Elbaz, D., Franco, M., et al. 2020, A&A, 642, A155
Zolotov, A., Dekel, A., Mandelker, N., et al. 2015, MNRAS, 450, 2327